1 **Gravity Effect of Alpine Slab Segments Based on Geophysical and Petrological Modelling**

2 Maximilian Lowe [1,2,3], Jörg Ebbing [1], Amr El-Sharkawy [1,4], Thomas Meier [1]
3
4 [1] Institute for Geosciences, Kiel University, Germany
5 [2] NERC British Antarctic Survey, Cambridge, United Kingdom
6 [3] School of geosciences, University of Edinburgh, United Kingdom
7 [4] National Research Institute of Astronomy and Geophysics (NRIAG), 11421, Helwan, Cairo, Egypt
8
9 Correspondence to Maximilian Lowe: maxwe32@bas.ac.uk

11 **Abstract**

12 In this study, we present an estimate of the gravity signal of the slabs beneath the Alpine
13 mountain belt. Estimates of the gravity effect of the subducting slabs are often omitted or
14 simplified in crustal scale models. The related signal is here calculated for alternative slab
15 configurations at near surface height and on a satellite altitude of 225 km.
16 We apply three different modelling approaches in order to estimate the gravity signal from the
17 subducting slab segments, by: i) Direct conversion of upper mantle seismic velocities to density
18 distribution, which are then forward calculated to obtain the gravity signal. ii) Definition of slab
19 geometries based on seismic crustal thickness and high-resolution upper mantle tomography
20 for two competing slab configurations. The geometries are then forward calculated by assigning
21 a constant density contrast and slab thickness. iii) Accounting for compositional and thermal
22 variations with depth within the predefined slab geometry.
23 Forward calculations predict a positive gravity signal of up to 40 mGal for the Alpine slab
24 configuration. Significant differences in the gravity anomaly patterns are visible for different
25 slab geometries in the near surface gravity field. However, different contributing slab segments
26 are not easily separated, especially at satellite altitude. Our results demonstrate that future
27 studies addressing the lithospheric structure of the Alps should have to account for the
28 subducting slabs in order to provide a meaningful representation of the geodynamic complex
29 Alpine area.
30
31 Keywords:
32 Satellite gravity gradient, Alpine subduction, lithospheric and sub lithospheric structure, mantle
33 composition, seismic tomography

1. Introduction

Interpretation of gravity anomalies can reveal information on the architecture and tectonic

setting of the lithosphere (e.g. Zeyen, & Fernàndez, 1994; McKenzie & Fairhead, 1997;

Holzrichter & Ebbing, 2006; Braitenberg, 2015; Spooner et al. 2019). For subduction zones,

like the Andes, several studies have shown that the gravity effect of the subducting plates is

significant and has to be considered in order to study the feedback between the subducting

lithosphere and the overriding plate (Götze et al. 1994; Götze & Krause 2002; Tašárová 2007

Gutknecht et al. 2014; Götze & Pail 2018; Mahatsente 2019). Subducting lithosphere has a

43   higher density than the surrounding mantle material at the same depth interval causing a

44   negative buoyancy and therefore the slab is subducted into earth's interior (e.g. Kincaid & Olson

45   1987; Ganguly et al. 2009). However, the gravitational contribution of subducting material in

46   the upper mantle to the gravity field has so far not been systematically addressed for the Alpine

47   system. In order to provide an assessment, the magnitude of the gravity signal of such sub-

48   crustal long wavelength features has to be estimated.

49   The Alpine mountain belt (Fig. 1a) is chosen for this sensitivity study because firstly a large

50   range of recent seismic topography studies imaged subducting slab segments in the Alpine

51   region (e.g. Babuska et al., 1990; Lippitsch et al., 2003; Spakman & Wortel, 2004; Mitterbauer

52   et al. 2011; Karousova et al., 2013; Zhao et al., 2016; Kästle et al., 2018; El-Sharkawy et al.,

53   2020). Those different studies suggest different configurations of slab segments (see section

54   1.1), allowing us to test how sensitive the gravity field is to varying geometries of subducting

55   slab segments. Secondly, previous Alpine models addressing the Alpine gravity field have not

56   considered any slab segments, rather they only account for the thickness of the lithosphere (e.g.

57   Ebbing et al., 2006; Spooner et al., 2019; Tadiello and Braitenberg 2020). If the contribution of

58   the slab is not considered, a significant part of the gravity field might be attributed to crustal

59   thickness variations or intra-crustal sources.

60   In addition, the Bouguer Anomaly of the Alps (Fig. 1b) shows no direct sign of subducting slabs

61   (in contrast to the Andes subduct zone) as the field is dominated by crustal thickness variations

62   (Ebbing et al., 2001, 2006) Therefore, forward modeling of the proposed slab geometries, as

63   imaged by high-resolution tomographic studies, is neccesary to separate the gravity signal

64   caused by the suducting slabs from the gravity anonaly field.
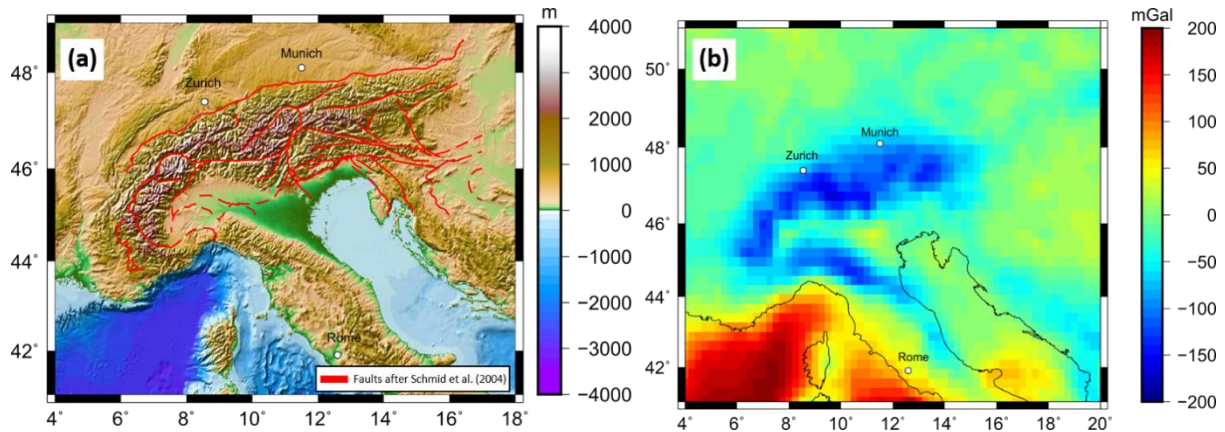
Figure 1 (a) Topography from ETOPO1 from Amante and Eakins (2009). Faults in red after Schmid et al. (2004). (b) Bouguer Anomaly based on XGM 2019 with a maximum spherical harmonics degree of 719 at a station height of 6040m above the ellipsoid, just above the surface of the Alps. Correction density for rock: 2670 kg/m³ and for water: 1030 kg/m³

We present three different approaches to model the gravity effect of the slab segments and discuss the strengths and limitations of the applied methods. In the first approach, the alpine sup-crustal density distribution is derived by converting seismic velocities to density. This model is then forward calculated to estimate the gravity response. In the second approach, 3D slab geometries are derived by evaluating seismic crustal thickness estimations and high-resolution upper mantle tomographic models. Here, two competing slab configurations are chosen. The predefined slab geometries are then forward calculated by assigning different density contrast and slab thicknesses. The third approach uses similar predefined slab configurations as in the second approach, however, here we consider petrology, temperature, and density variation. The gravity response is calculated for all three approaches at a near surface height for the gravity disturbance and the gravity gradients at satellite altitude of 225 km.

1.1 Alpine setting

The formation and present geodynamics of the Alps are linked to long lasting tectonic processes, including Adria-Europe continent-continent collision, subduction of oceanic and continental lithosphere, the formation of crustal nappes as well as extensional and compressional processes (Frisch, 1979; Stampfli & Borel, 2002; Handy, et al., 2010, 2015). The Adriatic microplate is a major driver of the present geodynamics in the Alpine region, which is trapped between the converging major plates of Europe and Africa. Adria is moving

88   counterclockwise with respect to Europe, as seen by GPS observations (e.g. Nocquet and Calais,

89   2004; Vrabec and Fodor, 2006; Serpelloni et al., 2016) and is subducted beneath the Apennines to

90   the west as well as to the east beneath the Dinarides, while colliding with Eurasia in the Alps

91   to the north (e.g. Channel & Horvath, 1976; Dewey et al., 1989; Stampfli & Borel, 2002; Handy

92   et al., 2010; Le Breton et al., 2017). Subducting slab segments have been imaged by different

93   seismological body wave travel time tomographic studies as well as surface wave tomographic

94   studies within the Alpine upper mantle (e.g. Babuska et al., 1990; Lippitsch et al., 2003;

95   Spakman & Wortel, 2004; Mitterbauer et al. 2011; Karusova et al., 2013; Zhao et al., 2016;

96   Kästle et al., 2018; El-Sharkawy et al., 2020). However, the configuration of subducting slab

97   segments remains controversial. In the Western Alps, Lippitsch et al. (2003) propose a slab

98   break-off at about 100 km depth, which is in line with the findings of Beller et al. (2018), Kästle

99   et al. (2018) and El-Sharkawy et al. (2020). In contrast, a continuous subducting slab segment

100 in the Western Alps, down to at least 250 km depth, is imaged by a number of other tomographic

101 models (e.g. Koulakov et al., 2009; Zhao et al., 2016; Hua et al., 2017; Lyu et al., 2017).

102 A continuous subduction of Eurasia beneath the Central Alps down to at least 200 km depth is

103 imaged by different tomographic models (e.g. Lippitsch et al., 2003; Piromallo and Morello,

104 2003; Koulakov et al., 2009; Mitterbauer et al., 2011; Hua et al., 2017; Fichtner et al., 2018; El-

105 Sharkawy et al., 2020). A potential slab gap with an approximately size of 2° is separating the

106 subducting slab segments in the Central Alps to the Eastern Alps as imaged by e.g. Lippitsch

107 et al. (2003). The slab configuration and subduction direction in the Eastern Alps remains

108 unclear. According to the classical view, Eurasia is subducting beneath Adria in a southward

109 subduction (Hawkesworth et al., 1975; Lüschen et al., 2004; 2006). This idea was challenged

110 by Lippitsch et al. (2003), Schmid et al. (2004), Kissling et al. (2006), Handy et al. (2015), and

111 Hetenyi et al. (2018). Instead, slab break-off in the eastern Alps and a northward-dipping

112 Adriatic slab in the easternmost Alps is suggested, leading to a switch of the slab polarity, as

113 Adria is subducting beneath the European plate (Handy et al., 2015). The view that Adriatic and

114   not Eurasian lithosphere is subducting northwards in the Eastern Alps has been opposed by

115   Mitterbauer et al. (2011), as their model shows a northward dipping slab in the eastern most

116   Alps connected to the European plate. In an early tomographic study, Babuska et al. (1990)

117   proposed that both Eurasian and Adriatic lithosphere is subducting in the eastern Alps. In

118   subsequent studies and interpretations this model was mentioned but northward subduction of

119   Adria seems to be favoured (e.g. Karousova et al., 2013; Hetenyi et al., 2018), Recently,

120   subduction of both Eurasian and Adriatic lithosphere in the eastern Alps down to about 150 km

121   has been suggested by Kästle et al. (2020) and El-Sharkawy et al. (2020) based on surface wave

122   studies. For a more in-depth comparison and discussion of tomographic Alpine models the

123   reader is referred to e.g. Kästle et al. (2020).

124   **2. Data**

125   The Bouguer Anomaly (Fig. 1b) is based on the global model *XGM 2019* (Zingerle et al., 2019)

126   developed for spherical harmonics up to degree 719, with a resolution of ~25 km (half

127   wavelength). The XGM 2019 model is a global integrated gravity model, which includes

128   satellite and terrestrial measurements. The simple Bouguer Anomaly is calculated from the

129   Free-Air gravity disturbance with a correction density of 2670 kg/m^3 for topography, and a

130   correction density for water of 1030 kg/m^3 for the offshore areas. We calculated the gravity

131   contribution of the topography and bathymetry using Tesseroids and subtracting the signal

132   proportion from the Free-Air Anomaly to obtain the Bouguer Anomaly. For the topography and

133   bathymetry information, we use ETOPO1 with a 1 arc minute resolution (Amante & Eakins,

134   2009), which was regrided at a regular grid with a grid space of 25 km to match the resolution

135   of the XGM 2019 model for a maximum degree of 719. The gravity field is defined at a constant

136   station height of 6040 m above the ellipsoid, just above the surface of the Alps. The resulting

137   Bouguer Anomaly shows a gravity low in the order of -200 mGal over the high topography of

138   the Alps, indicating an isostatic compensation of the topography (e.g. Ebbing et al., 2006).

139   Additionally, we calculate the topographic correction for the gravity gradients at a station height

140   of 225 km representing the GOCE satellite altitude. The topographic corrected gravity gradients

141   after Bouman et al. (2016) measured by the GOCE ESA satellite mission are presented in the

142   appendix.

143   For the definition of the slab geometry, we use crustal thickness estimates based on the receiver

144   function study by Spada et al. (2013). The crustal thickness map was digitized and the Moho

145   gap in the eastern Alps is filled by nearest neighbour interpolation. To avoid edge effects,

146   surrounding areas are supplemented by the Moho depth model of the European plate by Grad

147   et al. (2009), both data sets were merged using a cosine taper with a taper width of 2° using

148   equation (1). The overlapping areas at the grid edges are distance weighted to obtain a smooth

149   transition.

150    $$G_{new} = T(x,y) \cdot G_1(x,y) + \big(1 - T(x,y)\big)G_2 \cdot (x,y)) \quad (1)$$

152    $$with: T(x,y) = cos\frac{D \cdot \pi}{2 \cdot L}$$

151   *with: G = Grids, T = taper, D =dx, L = Tapper length*

153   The merged Moho depth map is sampled at a regular grid with a cell size of 0.25° (Fig. 2) to be

154   consisted with resolution of the topographic and gravity models.
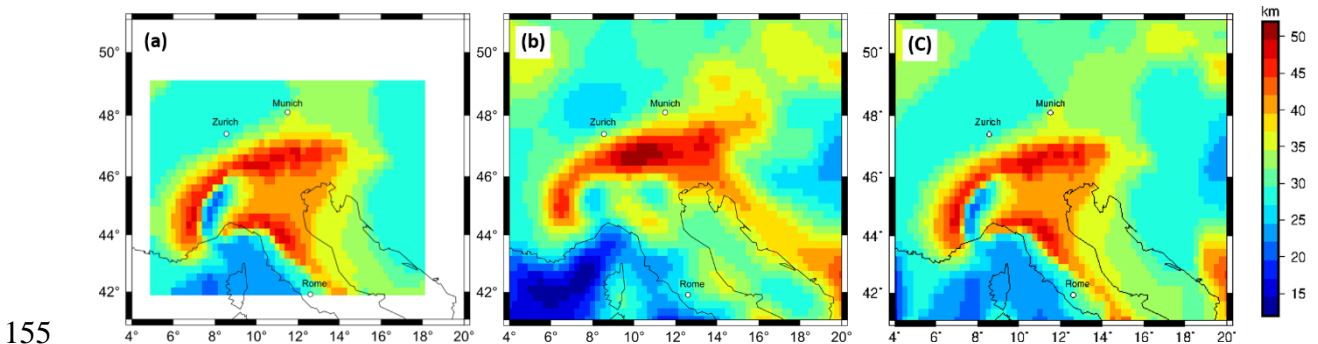
155

156 *Figure 2 a) digitized crustal thickness after Spada et al. (2013) with a 0.25 ° grid spacing, b) crustal depth estimation after*
157 *Grad et al. (2009) with a 0.25 ° grid spacing c) Merged crustal thickness map from Spada et al. (2016) and Grad et al. (2009)*
158 *with a grid resolution of 0.25 ° using a cosine taper with a 2° width.*

159   For the upper mantle seismic velocity, the 3-D shear wave velocity model (MeRE2020) by El-

160   Sharkawy (2020) is used (Fig. 3). The model covers the upper mantle across the Alpine-

161   Mediterranean area down to a depth of 300 km and absolute shear-wave velocities are given.

162   In this study, relative shear-wave velocities in the depth range from 70 to 200 km are calculated

163   with respect to a 1-D average shear wave velocity model, the background model is descripted

164   in El-Sharkawy (2020). The upper limit of 70 km is introduced because i) we focus on the

165   contribution of the slab segments removing therefore crustal information from the model ii) the

166   tomography model MeRE2020 is not sensitive to shallow structures, as a result the slabs are

167   not well recovered in depths shallower than 70 km iii) we want to ensure a uniform upper

168   boundary. The lower boundary of 200 km is chosen based on clear images of the Alpine Slab

169   segments to at least 200 km depth (with exception of the Western Alpine slab), as discussed in

170   section 1, and the assumptions that depth larger than 200 km will have a negligible effect on

171   the regional gravity field considered here.

172   The ambient noise tomography by Kästle et al. (2018) is used to define the geometry of the

173   Western Alpine slab segment, hence we follow the idea of a slab-breakoff in the Western Alps

174   at 100 km depth (Kästle et al., 2020) as suggested also by Lippitsch et al. (2003) and Beller et

175   al. (2018). For the eastern Alps, we consider two alternative models. For the first hypothesis,

176   the P-wave tomography by Lippitsch et al. (2003) is used, to define the Eastern Alpine slab

177   segment. The second hypothesis is based on Kästle et al. (2020) and El-Sharkawy et al. (2020).

178   It assumes southward subduction of a short Eurasian Slab as well as northward subduction of a

179   short Adriatic Slab in the eastern Alps. The slab configurations which are incorporated in the

180   Alpine density models are discussed in greater detail in section 4.1.

181   **3 Conversion of seismic velocities into density distribution**

182   Seismic velocity variations are dependent on temperature and pressure. Densities in the

183   subsurface are also temperature and pressure dependent. A conversion factor (ζ) can describe

184   the linear relation between seismic velocities variations and densities variation (e.g. Tiberi et al.

185   2001; Webb 2009). We convert seismic shear wave velocities from the tomographic model

186   MeRE2020 by El-Sharawy et al. (2020) in the depth range from 70 to 200 km, as discussed in

187   section 2, to obtain a density distribution of the upper mantle in the Alpine region based on a

188   conversion factor (ζ). The relationship between seismic velocities and densities is described in

189   equation (2), this assumption is a strong simplification of reality, but gives a first order

190   estimation of the expected relative density structure beneath the Alps.

191     $$\rho_{rel} = [(Vsv_{abs} + \Delta\%) - Vsv_{abs}] \cdot \zeta \quad (2)$$

192     $with$: $Vsv_{abs} = absolute\ velocieties\ from\ MeRE2020;$

193     $\Delta\% = precentage\ divagation\ from\ the\ MeRE2020\ background\ model;$

194     $\zeta = conversion\ factor$

195   The result is strongly dependent on the chosen conversion factor. A range for conversion

196   factors has been proposed in the literature for different rock types ranging from 0.1 to 0.45 (e.g.

197   Isaac et al., 1989; Isaak, 1992; Karato, 1993; Kogan and McNutt, 1993; Vacher et al., 1998).

198   The relative shear-wave velocity distribution in a 3D domain from the tomography model

199   MeRE2020 from El-Sharkawy (2020) is converted using a constant conversion factor (ζ) of 0.3.

200   The converted relative density distribution varies between -240 and 350 kg/m³. High

201   correlations between the structural pattern in the converted density distribution and the relative

202   seismic velocities are observed (Fig. 3), the similarity in the structure pattern is expected due

203   to the linear relationship we introduced here. The converted 3D relative density distribution

204   reflects the variation of seismic velocities in the Alpine lithosphere and therefore includes the

205   heterogeneities of the subduction slab segments, as seen by the tomographic models (Fig 3).

206   The relative density model is transferred into tesseroids with a horizontal expansion of 0.2° and

207   a vertical expansion of 3 km. The Tesseroid model is forward calculated in order to estimate the

208   gravity response of the converted density distribution of the Alpine lithosphere in the depth

209   interval of 70 km to 200 km.

210
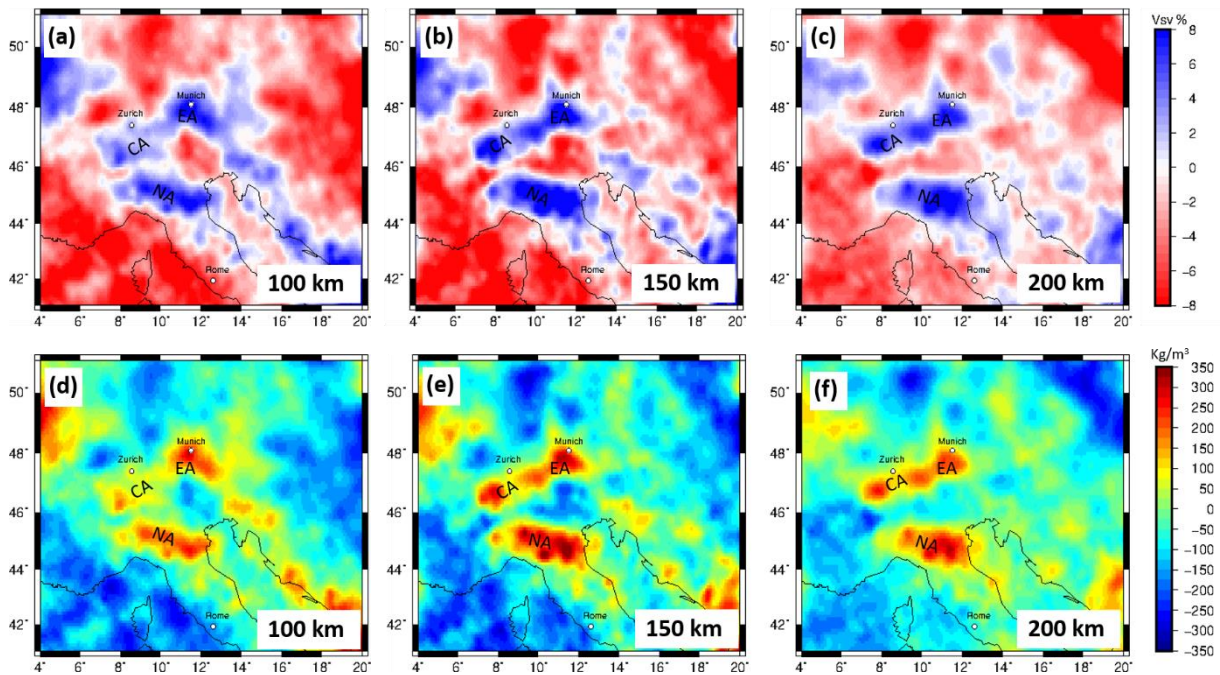
Figure 3 **(a)-(c)** Depth slices of relative surface wave velocities (Vsv) from MeRE2020 (El-Sharkawy et al., 2020). **(d)-(f)** converted relative density distribution in different depths based on a conversion factor (ζ) of 0.3. CA = Central Alpine Slab; EA = Eastern Alpine Slab; NA = Northern Apennine Slab

3.1 Results

In the forward calculated gravity field, a gravity high with a magnitude of ~40 mGal is observed

over the Alps (Fig. 4). That might be interpreted as relating to the proposed slab segments in

the Northern Apennine and Alpine area. However, the gravity field (and gradients, see appendix)

is dominated by anomalies outside the Alpine realm (Fig. 4), for instance in the Ligurian Sea

and the Dinaride-Hellenide Orogen. Therefore, in the next step, we try to concentrate on the

seismic anomalies in the Alpine realm that can be related to the slab segments.
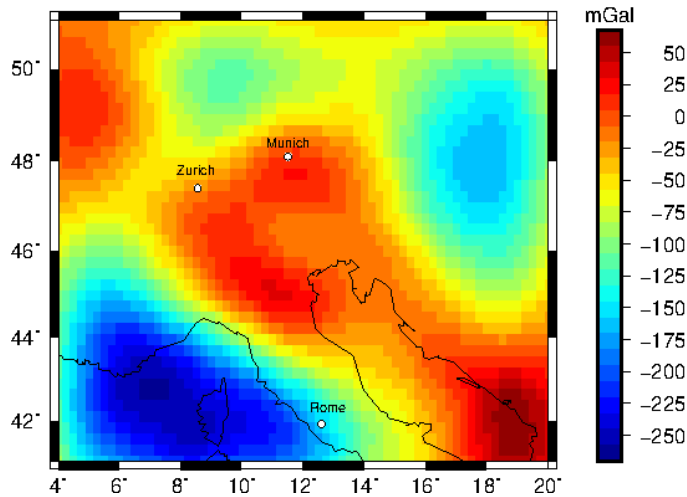
222

223 *Figure 4 Forward calculated gravity signal from relative density distribution converted from relative seismic velocities using*
224 *a conversion factor of 0.3 at a station height of 6040m.*

4 Slab models

225

226 To estimate the gravity contribution of independent slab segments we introduce different

227 models for the subducting lithosphere. First, we use a set of models with simple constant density

228 distribution in the slab, where the parameters, namely the density contrast and thickness of the

229 slab segment is varied (approach 2). Secondly, we create a set of slab models accounting for

230 compositional and thermal variations with depth (approach 3). Those models are created with

231 the software package LitMod 3D (Fullea et al., 2009) and will be referred as LitMod models in

232 the following. For all non-LitMod models, the gravity and gravity gradients are calculated using

233 tesseroids, which are spherical prisms (Uieda et al., 2016).

4.1 Slab modelling with constant density contrast and slab thickness

235 We define two alternative slab configurations based on crustal thickness model by Spada et al.

236 (2013) and several different tomographic studies, see detailed description of the slab

237 configurations below. At different depths, isolines are picked in the crustal depth map and

238 tomographic images, defining the upper boundary of subducting slab segments. The isoline of

239 the crust mantle boundary (Moho interface) is used as an onset of the slab to the crust and

240 defines the upper boundary of the subduction slab segment. At upper mantle depth, increased

241 seismic velocity anomalies in tomographic models beneath the Alps are interpreted as contrast

242 between colder and therefore denser subducting material to the surrounding mantle material. At

243 100, 150, and 200 km depth, the upper boundary of the slab segment is defined at the 0%

244 contour line of the relative seismic velocity, marking the transition from rocks with low velocity

245 to high velocity rocks. The isolines at the Moho interface, 100 km, 150 km and 200 km depth

246 are displayed upon the Alpine topography (Fig. 5 a-b) Vertical interpolation between the upper

247 boundary isolines at different depths (Moho depth, 100, 150 and 200 km) define a continuous

248 surface of the upper slab boundary. The lower boundary of the slabs and therefore the thickness

249 of the slab segment is not picked based on seismic data but assumed to have constant

250 thicknesses for simplifications. The thickness is varied for different models from 60 to 100 km

251 depth.
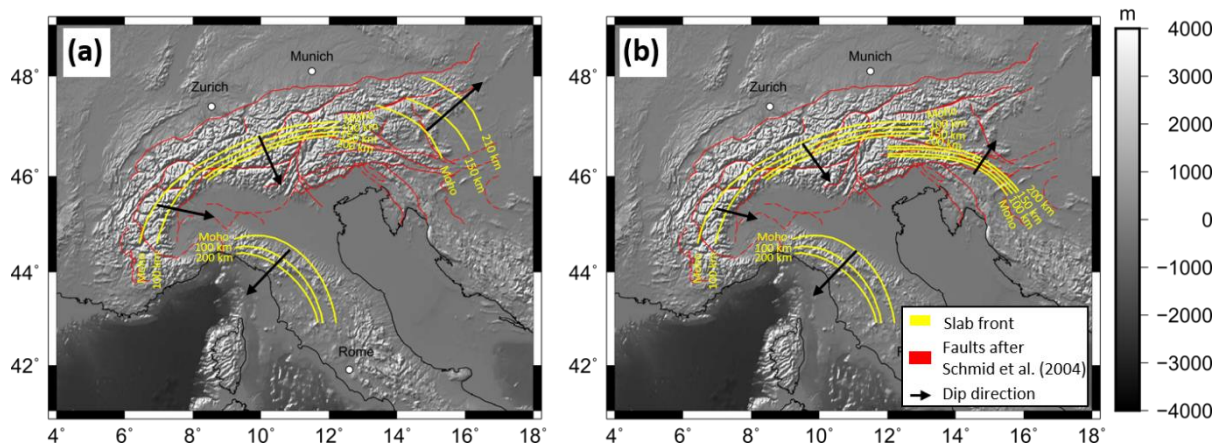
252

253 *Figure 5 Defined isolines based on crustal thickness estimations and seismological tomography models for the upper slab*
254 *boundary for **(a)** Configuration 1 and **(b)** Configuration 2. Black arrows indicate the subduction direction. In red the fault*
255 *configuration after Schmid et al. (2004).*

256 3.1.1 Alternative slab configurations
257 We define two different slab configurations. Configuration 1 (Fig. 5a) features a northeast

258 subducting slab segment in the Eastern Alps based on Lippitsch et al. (2003). A Central Alpine

259 slab segment is defined based on Lippitsch et al. (2003) and MeRE2020 (El-Sharkawy et al.,

260 2020) subducting in south-southeast direction. The Eastern and Central Alpine slab segments

261 are separated by a slab gap and show perpendicular subduction directions. The east-southeast-

262 ward subducted slab segment in the Western Alps is defined using the tomographic model of

263 Kästle et al. (2018), supporting the idea of slab break-off at about 100 km depth. Only attached

264 slab segments are considered, ignoring potential mantle upwelling in the break off zone and

265 neglecting the potentially remaining detached slab segment in larger depths. In addition, a

266 southwest-subducting slab segment beneath the northern Apennines is considered down to

267 about 200 km depth, as imaged by MeRE2020 (El-Sharkawy et al., 2020) because of its

268 proximity to the western Alps.

269 Configuration 2 (Fig. 5b) considers a slab configuration mainly based on the interpretation of

270 the MeRE2020 model (Fig. 3) by El-Sharkawy et al. (2020). In the Eastern Alps, both a short

271 southward subducting Eurasian slab segment as well as a short northward subducting Adriatic

272 slab are assumed. The Central and Western Alpine slab segments as well as the slab beneath the

273 northern Apennines are identical to Configuration 1.

274 4.1.2 Forward calculation
275 To estimate the gravity effect of the slab configurations, the geometries are discretized into

276 tesseroids with a 0.2° extension in the horizontal domain and a vertical size of 20 km. The

277 tesseroids range from 40 km to 200 km depth. First, a constant density contrast is assigned to

278 the entire slab. We test density contrasts from 20 kg/m^3 to 80 kg/m^3. The thickness of the Alpine

279 slab is not well constrained. We test for three slab volumes by assigning three slab thicknesses,

280 60 km, 80 km and 100 km based on studies on other subducting slab segments (e.g. Wang et

281 al., 2020). Due to the curved geometries of the proposed slab segments rectangular tesseroids

282 with a horizontal expansion of 0.2° will either over- or under-estimate the volume of a

283 subducting slab at the edges of the slab. The percentage volume share of each tesseroid to the

284 slab geometry is calculated. The assigned density contrast of the tesseroids which does not lay

285 fully within the slab geometry is decreased according to the percentage volume within the slab

286 geometry. Therefore, the density distribution correlates to the hypothetical slab positions and

287 volumes in the Alpine subsurface without increasing the discretisation resolution of the

288 tesseroid model beyond the uncertainty of gravity measurements and seismic tomographies.

289 The offset between the 40 km upper tesseroid boundary to the slab onset at the crust in 44 km

290 depth is corrected using the same process.

291 ### 4.1.3 Results

292 Forward calculated slab models for predefined slab geometries of Configuration 1 and 2 with a

293 constant density contrast of 60 kg/m^3 and a constant thickness of 80 km result in a sharp gravity

294 signal ranging from 70 mGal to 100 mGal (Fig. 6). Both models generate gravity signals in the

295 order of magnitude of 70 mGal in the Central Alpine region as well as in the Apennine. The

296 gravity signal in the Eastern Alps differ for the two hypotheses (Fig. 6 a, b). The Western Alpine

297 slab segment shows the weakest signal in both models.

298
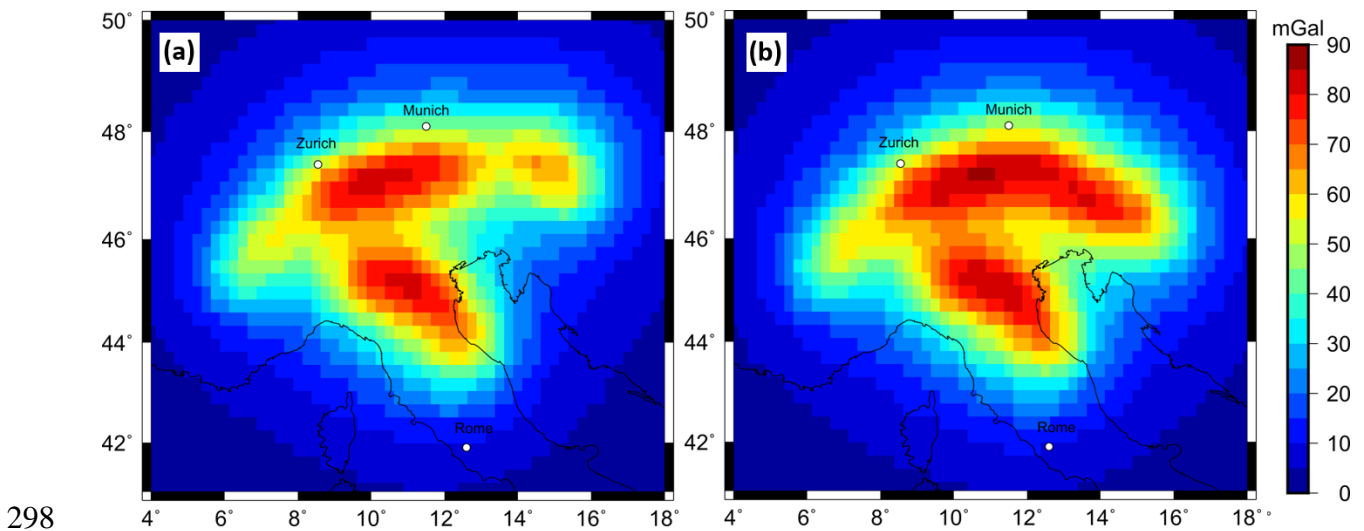
299 *Figure 6 Forward calculated gravity disturbance signal at a station height of 6040 m for predefined sub-crustal slab geometries*
300 *with a content density contrast of 60 kg/ m^3 and a constant thickness of 80 km. (a) predefined slab configuration 1 (b) predefined*
301 *slab configuration 2..*

302 The gravity signal ranges from 30 to 110 mGal depending on the assigned density contrast and

303 thickness for both slab geometry models (Fig. 7). The highest magnitude of forward calculated

304 gravity signal is in the order of 110 mGal and is observed for a slab model with a density

305 contrast of 80 kg/m^3 and a constant slab thickness of 100 km, while the lowest signal is

306 produced by a combination of 20 km/m^3 density contrast and a slab thickness of 60 km. Similar

307 gravity response is produced by different combinations of density contrast and volume. The

308 signal pattern is influenced by the predefined slab geometry, while the magnitude of the gravity

309 signal is depending on the density contrast and thickness (Fig. 7).

310
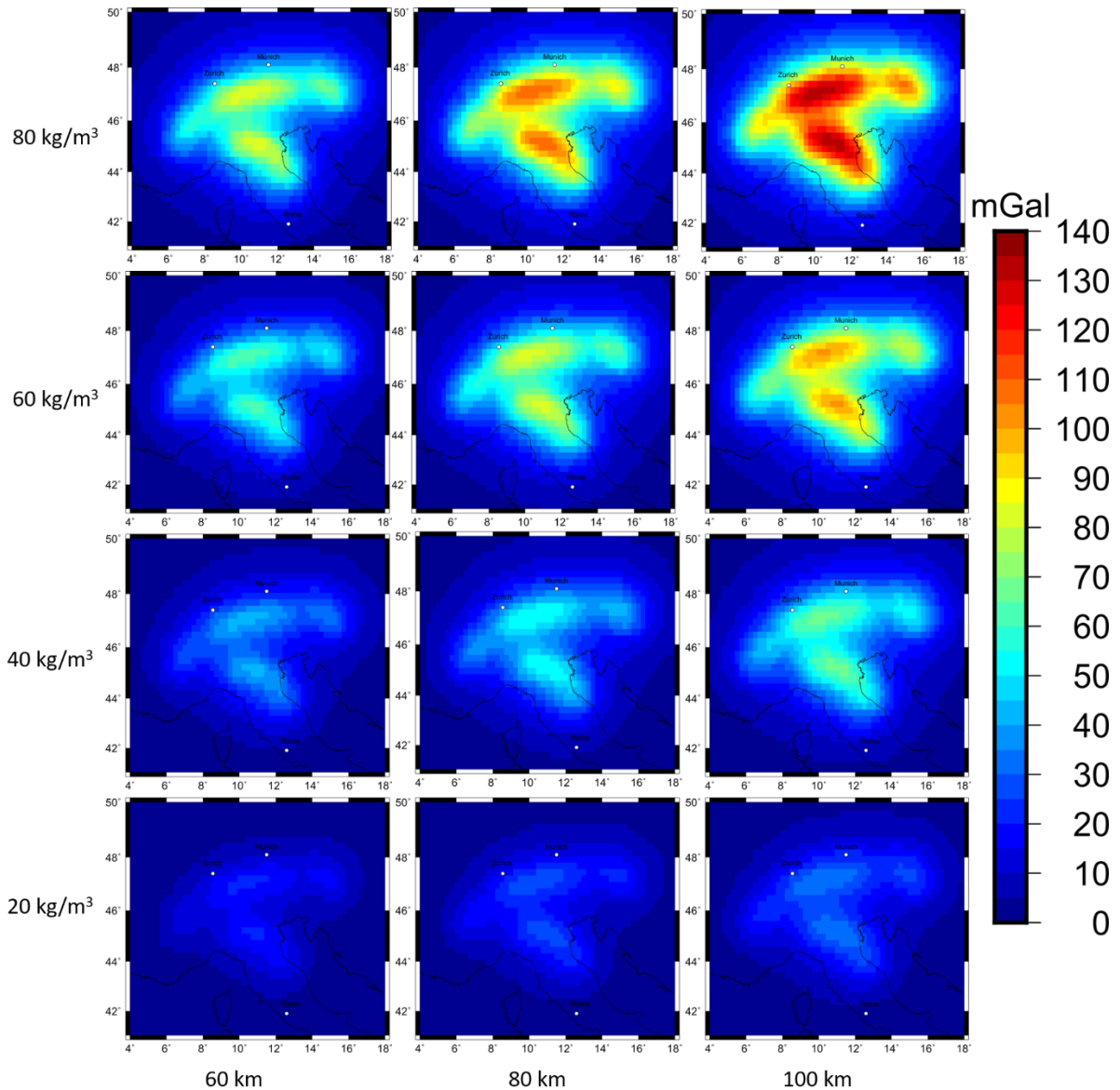
Figure 7 Forward calculated gravity disturbance signal for 12 different combination of density contrast and slab thickness for sub-crustal slab configuration 1 at a station height of 6040 m.

Forward calculated gravity gradients at satellite height show the same dependency of signal strength (see Appendix).

4.2 Geophysical and petrological modelling with LitMod

For modelling the Alpine slab segments taking temperature and pressure variations as well as composition of the lithosphere and sub lithosphere into account, the geophysical and petrological modelling software LitMod 3D is utilized (Fullea et al.,2009). LitMod 3-D is a finite difference code, which allows the modelling of lithospheric and sub lithospheric

320 structures down to 400 km depth by solving the heat transfer, thermodynamical, rheological,

321 geopotential, and isostasy equations (Afonso et al., 2008; Fullea et al., 2010).

322 A LitMod model consists of a set of crustal, lithospheric- and sub lithospheric layers

323 characterized by their petrophysical and thermal properties, which are used as input data (Fullea

324 et al., 2010). LitMod provides as an output i.e. the density -, temperature-, pressure- distribution

325 as well as the forward calculated gravity disturbance and gravity gradients (Fullea et al. 2009).

326 The assigned composition for the different layers is calculated using a LitMod subroutine which

327 utilizes the Perple_X algorithm of Connolly (2009). Perple_X calculates in the LitMod

328 implementation the specific bulk rock properties based on the six main lithospheric oxides

329 (SiO_2, Al_2O_3, FeO, CaO, Na_2O) by minimizing Gibbs free energy equation. The Alpine

330 lithosphere and sub lithosphere as well as the proposed slab segments are modelled using

331 standard global lithospheric and sub lithospheric compositions to test the influence of

332 compositional variations within the slab segments on the gravitational signal. Here, we use the

333 so-called Tecton and Proterozoic type-composition (Table 1). Those compositions were chosen

334 for a model with a homogeneous crust, lithosphere and sub-lithosphere, where the density

335 changes as a function of temperature and pressure based on the assigned compositions. The

336 different slab composition is introduced to test whether a compositional contrast, in addition to

337 the expected thermal difference, results in a significant density contrast between the slab and

338 the surrounding material.

339 *Table 1: Mineralogical composition for the lithospheric and sub lithospheric structure.*

Major Oxide Compositions	Aver. Tecton Gnt. SCLM [a]	Aver. Tecton Gnt. Peridotite [a]	Average Proterozoic Massif	PUM [b]	DMM [c]
SiO_2	44.5	45	45.2	45	44.7
Al_2O_3	3.5	3.9	2	4.5	3.98
FeO	8	8.1	7.9	8.1	8.1
MgO	39.8	38.7	41.6	37.8	37.8

CaO	3.1	3.2	1.9	3.6	3.17
Na₂O	0.26	0.24	0.13	0.36	0.13

[a] Classifications according to Griffin et al. (1999b), [b] McDonough & Sun (1995), [c] Workman & Hart (2005) DMM = Depleted mid-oceanic ridge basalt mantle, PUM = primitive upper mantle.

First, we create a reference model (M₀) without a slab segment. This model contains topography from the ETOPO1 dataset (Amante and Eakins, 2009), the Moho depth from Spada et al. (2013) and Grad et al. (2009). The lithosphere asthenosphere boundary (LAB) is a required interface for the LitMod 3D to divide the model between the lithosphere and sub lithosphere and to assign compositions. We introduce a fixed technical LAB at a depth of 100 km throughout the model despite of the presence of slabs as the LAB is defined as the 1300°C isotherm. This set-up avoids that the isotherm follows the geometrical shape of the slab, which would lead to a location in unrealistic large depths (>200 km). In addition, we neglect the topography of the LAB for several reasons: i) the information of the lithospheric thickness in the Alpine forelands is spare and under ongoing discussions, ii) the fixed depth value is based on thermal isostasy LAB estimations from Artemieva et al. (2019), which shows a LAB depth in the range of 80 to 120 km depth in the Alpine forelands. This technical LAB is used to parameterize the model and is not meant to represent the topography of the LAB.

Slab segments are introduced stepwise for the lithosphere and sub lithosphere domains into the model as well as thermal anomalies for the slab segment beneath the technical LAB, which describes the 1300°C isotherm (Table 2). Calculating the difference to the reference model (M₀) allows to estimate the effect a slab segments has on the density, temperature distribution of the Alpine subsurface and therefore on the Alpine gravity field based on slab position, slab geometry and composition.

Table 2: Different LitMod models and there incorporated lithospheric and sub lithospheric structures and compositions.

Models	Slab geometries	Slab composition (mantle)	Mantle composition	Slab composition (sub lithosphere)	Sub lithosphere composition	Thermal anomaly within sub lithospheric slab

M$_0$	-	-	aver. Tecton Gnt.	-	PUM	-
M$_1$	Configuration 1	Aver. Tecton Gnt. Peridotite	aver. Tecton Gnt.	-	PUM	-
M$_2$	Configuration 2	Aver. Tecton Gnt. Peridotite	aver. Tecton Gnt.	-	PUM	-
M$_3$	Configuration 1	Aver. Tecton Gnt. Peridotite	aver. Tecton Gnt.	DMM	PUM	-100 °K
M$_4$	Configuration 2	Aver. Tecton Gnt. Peridotite	aver. Tecton Gnt.	DMM	PUM	-100 °K
M$_5$	Configuration 1	Aver. Tecton Gnt. Peridotite	aver. Tecton Gnt.	PUM	PUM	-
M$_6$	Configuration 1	Aver. Tecton Gnt. Peridotite	aver. Tecton Gnt.	DMM	PUM	-
M$_7$	Configuration 1	Aver. Tecton Gnt. Peridotite	aver. Tecton Gnt.	DMM	PUM	-200 °K
M$_8$	Configuration 2	Average Proterozoic Massif	aver. Tecton Gnt.	-	PUM	-

362   A positive density contrast between subducting material and the surrounding mantle material

363   results in a negative buoyancy force. A density contrast is introduced into the LitMod model by

364   a difference in composition between the subducting denser slab and the surrounding mantle

365   (Fig. 9). Here, we use Tecton like compositions for the lithosphere and the subducting slab

366   segments since the Alpine slab segments result from continent-continent collision (Tables 1 and

367   2). A later model features a Proterozoic slab composition (M$_8$). Depleted mid-oceanic ridge

368   basalt mantle (DMM) and primitive upper mantle (PUM) are used for the sub lithospheric

369   domain. Additional to the density contrast within the sub lithosphere, a temperature anomaly of

370   – 100 K is introduced for the sub lithospheric part. Later models include a variation of

371   temperature anomalies (M$_5$, M$_6$, M$_7$). Note those compositions are used as a first order test and

372   serve as a starting point for synthetic slab models to illustrate the compositional and thermal

373   effect on the gravity signal by influencing the density distribution. They do not necessary

374   represent the compositional mantle environment in the Alpine region.
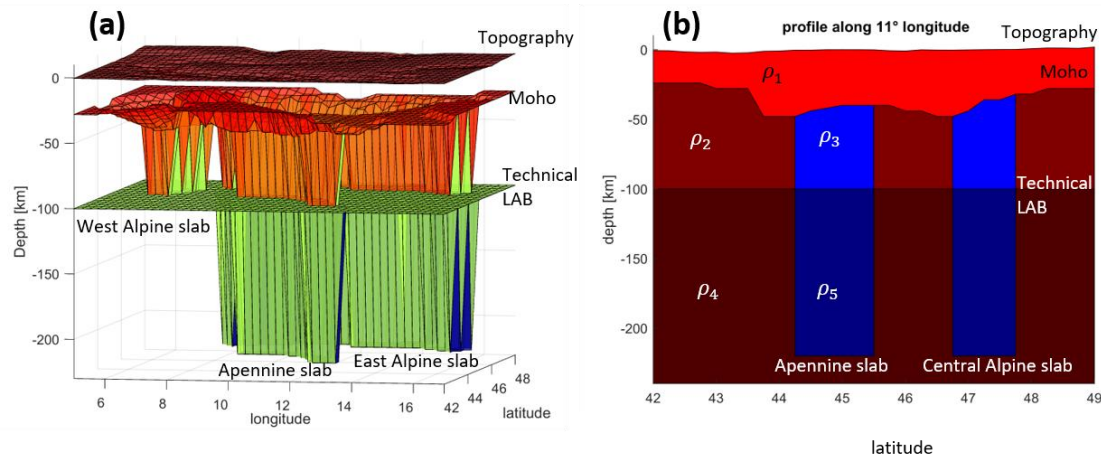
Figure 8 **(a)** 3D model set up using LitMod 3D. Topography, Moho and LAB depth as well as the vertical incorporated slab models are used as input layers with assigned petrophysical and thermal properties. **(b)** Profile along 11° longitude through a LitMod model containing Topography, crustal and lithospheric thickness as well as a slab segment. rho_{1-5} indicate petrophysical and thermal property variations for each layer.

4.2.1 Results

The gravity signal of the predefined slab segments is forward calculated as well as the background model without incorporation of slab segments. The residual between both forward calculations gives the gravitational contribution of the slab segments, while other gravitational effects, like the topography or crustal thickness variation are not considered.

A slab segment with an average Tecton Gnt. composition (M_1, M_2) results in a slightly denser material compared to the surrounding mantle (M_0), while a slab segment with a Proterozoic composition (M_8) shows a less dense lithospheric structure compared to the reference model (M_0), this composition results in less dense slab segment, which would not be subducted due to the positive buoyancy (Fig. 10). However, we aim to illustrate the effect composition has on the density distribution within the slab and to the surround mantle and show the importance of correct compositional information, therefore we focus on the difference in density contrast between slab and surrounding mantle and neglecting the sign of the density contrast.
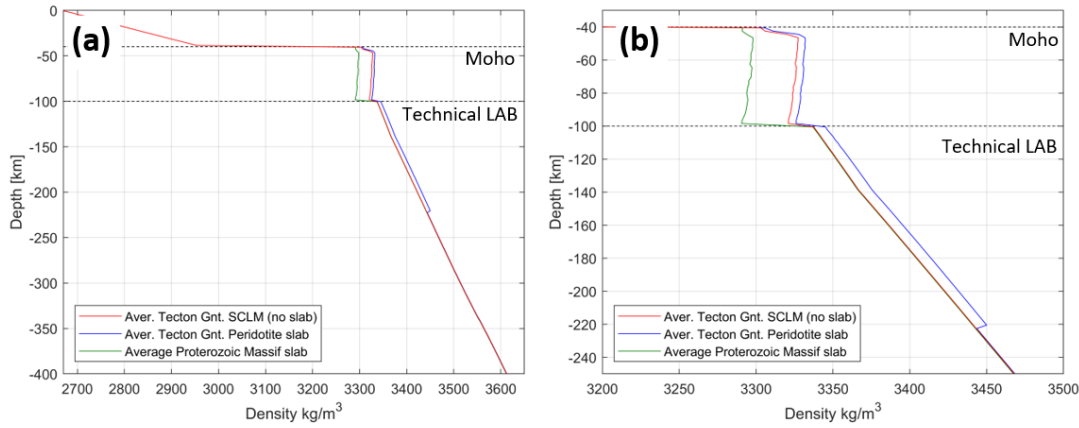
393

394 *Figure 9 (a) density profile at 11° longitude and 45° latitude for the full vertical model space of 400 km depth. Density profiles*
395 *for 3 different models (M₀, M₁, M₉) with different compositional properties are shown. (b) Zoomed in profile at the depth range*
396 *of present slab segments.*

397 The difference in density distribution (density contrast) within the slab segments with a Tecton

398 composition (M_1, M_3) to the reference model (M_0) is in the order of 5 kg/m³ for the lithosphere

399 and in the order of 10 kg/m³ for the sub lithospheric domain (Fig. 10a). The density variations

400 within the lithospheric and sub lithospheric slab domain are less than 1 kg/m³ resulting from

401 both depth dependent variations in pressure and temperature Between lithosphere and sub

402 lithosphere, a rapid increase in density contrast is observed (Fig. 10a). The density contrast of

403 a lithospheric Proterozoic slab composition (M_9) to the reference model (M_0) is in the order of

404 -30 kg/m³ (Fig. 10b).
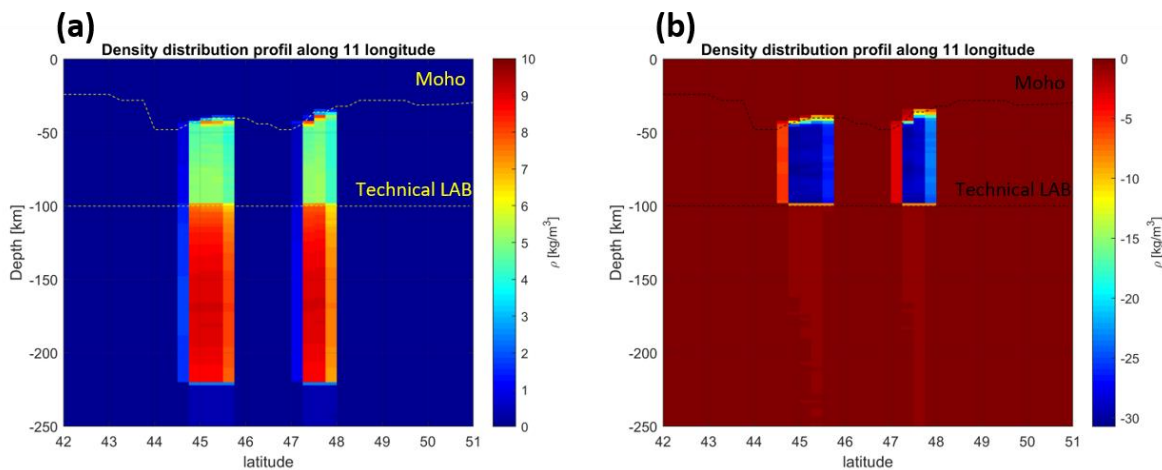
405

406 *Figure 10 (a) residual density contrast for lithospheric and sub lithospheric slab segments of model (M₃) with Tecton like*
407 *composition within the lithosphere and PUM and DMM composition in the sub lithosphere with an additional thermal anomaly*
408 *of -100° k for the sub lithospheric slab segment to the background model (M₀). (b) Residual lithospheric density contrast of a*
409 *Proterozoic lithospheric slab segment (M₈) to a Tecton compositional surrounding mantle (M₀). Residual density contrast is*
410 *limit to the technical LAB as the sub-lithospheric part is identical to the reference model (see also Fig. 9b)*

411   The gravity signal caused by the proposed slab segment configurations is estimated for

412   lithosphere and sub lithosphere separately. The forward calculated gravity effect, at topographic

413   surface level, for the slab configuration 1 for the lithospheric part is in the order of 4 mGal

414   while the sub lithospheric gravity signal is in the range of 7 mGal (Fig. 12a, b). The combined

415   gravity signal is in the order of 12 mGal (Fig. 12c). The gravity signal in the Eastern Alps for

416   Configuration 2 is significant larger in the order of 17 mGal for the combined model (Fig. 12f).
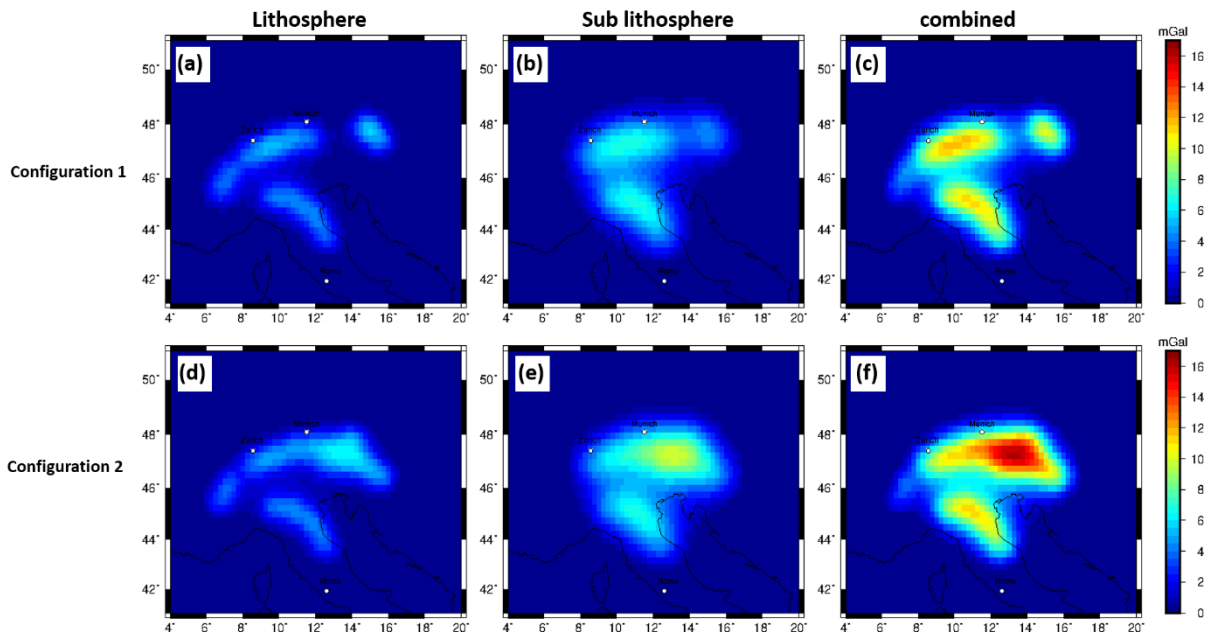
417

418   *Figure 11 Residual of the forward calculated gz gravity signal of lithospheric slabs at surface station height based on LitMod*
419   *models with Tecton like compositions in the lithosphere and PUM and DMM compositions in the sub lithosphere (M_1, M_2, M_3,*
420   *M_4,) with an additional thermal anomaly of -100° k for the sub lithospheric slab segment, for predefined slab Configuration to*
421   *the background model (M_0). (a)-(c) Configuration 1. (d)-(f) Configuration 2. Crustal and topographic contribution are nullified.*

422   The calculated gravitational effect of a slab segment with Proterozoic composition and a Tecton

423   surrounding mantle composition is in the order of -40 mGal for the gz component (Fig. 12 a).

424
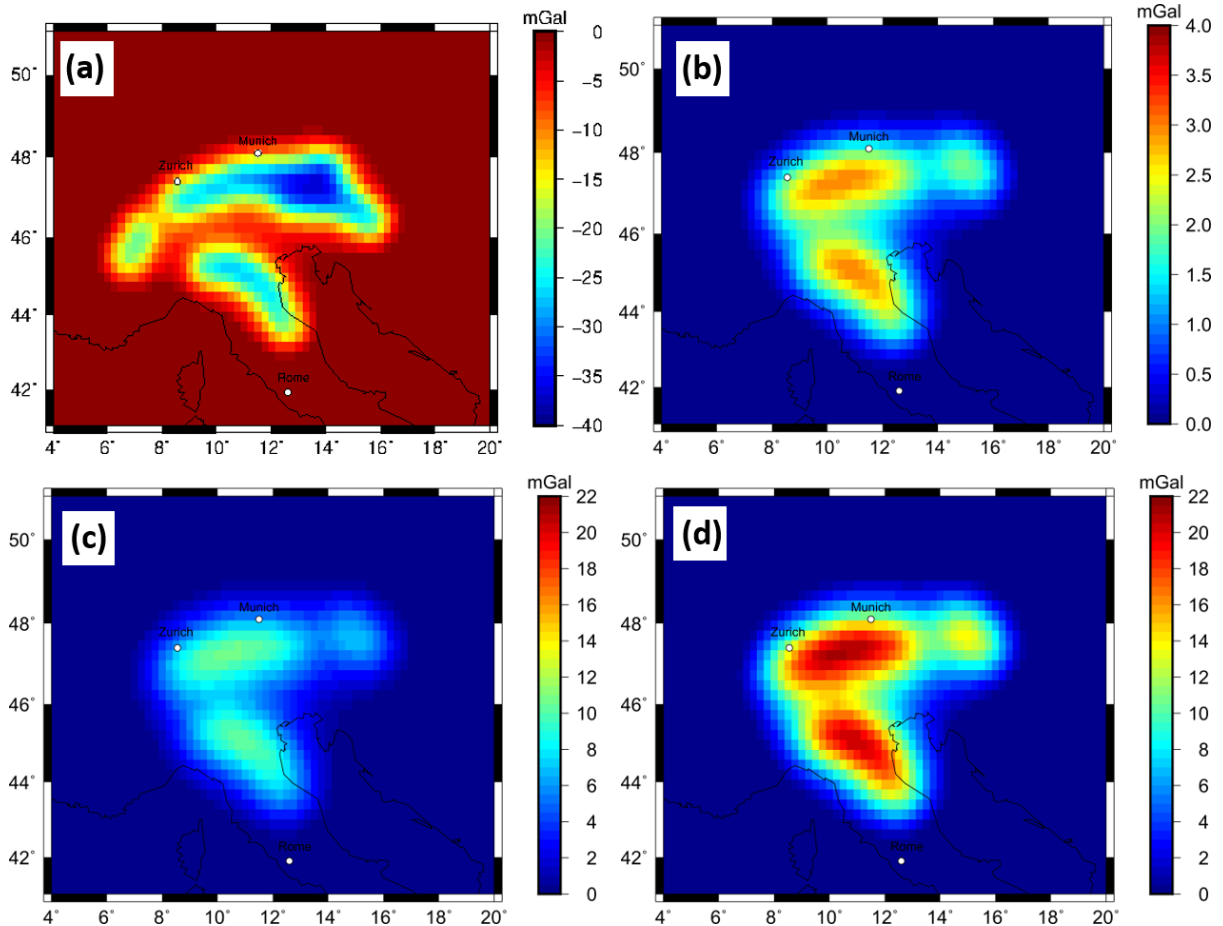
Figure 12 *(a) Forward calculated gravity effect of a Proterozoic lithospheric slab segment to a Tecton compositional surrounding mantle for configuration 2, obtained by calculating the residual between M_8 and M_0. (b) gravity signal produced by purely compositional effect in the sub lithosphere between a PUM and DMM composition, obtained by calculating the residual between M_5 and M_6. (c) gravity signal produced by purely thermal anomaly of -100° K for a sub lithospheric slab segment, obtain by calculating the residual between M_3 and M_6. (d) gravity signal produced by purely thermal anomaly of -200° K for a sub lithospheric slab segment obtained by calculating the residual between M_6 and M_7.*

431 The gravity response to a compositional variation within the sub lithosphere between the

432 incorporated slab segment (DMM composition) and the surrounding mantle (PUM composition)

433 is in the order of 4 mGal (Fig. 12b). The gravity response for a pure thermal anomaly of -100

434 K within the sub lithospheric slab segment is in the order of 16 mGal (Fig. 12c), while a pure

435 thermal anomaly of -200 K within the sub lithospheric slab segment is in the order of 21 mGal.

436 **5 Discussion**

437 The imprint of the gravity response caused by the density distribution based on direct

438 conversion of seismic velocities (approach 1) is visible, however, individual and independent

439 slab segments cannot be identified (Fig. 4). The strength of this approach is that it is fast to

implement and can provide a first order characterization of the gravity signal and slab geometries of subducting lithosphere. However, a clear characterization of subducting slab segments is not possible. First of all, the density model depends on the resolution and regularization of the seismological model, which can lead to distortions in the gravity response (e.g. Root, 2020). The method is dependent on the choice of the conversion factor and might overestimate the density (see the large negative anomaly in the Ligurian Sea). The conversion factor is a strong simplification of nature and for such a geodynamic complex area, a constant conversion factor is not adequate.

The forward calculated gravity field with competing predefined slab geometries (approach 2) shows a clear gravity signal, where the individual slab segments are distinguishable (Fig. 6).

A relative gravity low related to the slab gap in the Eastern Alps is a prominent feature in the gravity signal of Configuration 1 (Fig. 6a). The eastern Alpine slab segment of Configuration 1, due to its relatively small volume, result in a lower signal compared to the Central Alpine slab segment.

Configuration 2 shows a larger gravity signal in the Eastern Alps up to 100 mGal (Fig. 6b) compared to Configuration 1. The increase of the gravity signal is attributed to the subduction of both Eurasian and Adriatic lithosphere in the Eastern Alps. The gravity signal shows a continuous transition from the Central Alps to the Eastern Alps, where the contribution of the destined slab segment cannot be distinguished in the resulting gravity field (Fig. 6b). In the Western Alps, Configuration 1 and 2 show a lower gravity signal compared to the Central Alps. This is attributed to the much shallower Western Alpine slab segment that penetrate down to 100 km depth.

The gravity signal is influenced by both the assigned density contrast and thickness of the slab. A trade of between both parameters is clearly observable as the same gravity response of the slab configuration can be achieved with different values of density contrast and slab thickness.

465   Therefore, making it impossible to derive slab properties in form of density contrast and slab

466   thickness from the gravity field (Fig. 7).

467   The calculated densities in LitMod 3-D models (approach 3) are estimated taking temperature

468   and pressure variations into account based on an assigned composition. The composition has a

469   strong influence on the resulting density contrast. In the case that the compositional contrast

470   between slab segment and surrounding mantle is small, the density contrast is consequently

471   small as well (Fig. 9 and 10a). With increasing compositional differences, the density contrast

472   increases as well. A strong density contrast within the slab segment is recognizable between

473   lithospheric and sub lithospheric domain (Fig. 10a and b), while the variations between the slab

474   and surrounding mantle remain small.

475   The gravity signal shows in the Eastern Alps significant larger signal from the lithosphere and

476   sub lithosphere domain for Configuration 2 (Fig. 11d, e, and f) compared to Configuration 1

477   (Fig. 11a- c). The different slab segments are distinguishable with the exception of the two slab

478   segments in the Eastern Alps in Configuration 2 (Fig. 11). The contribution from the

479   lithospheric domain to the gravity signal is smaller than from the sub lithospheric domain (Fig.

480   11b, and e). However, the slab gap and the eastern slab segment feature can be recognized in

481   the lithospheric part in Configuration 1 but not in the gravity signal of the full model.

482   The Proterozoic slab segment has a larger gravity response compared to the Tecton-like

483   composition. This gravitational signal is negative due to the less dense Proterozoic composition

484   in comparison to the reference model (M_0) (Fig. 12a).

485   Sub lithospheric composition has only a small influence on the gravity field, in the order of 4

486   mGal (Fig. 12b). However, a thermal anomaly within the sub lithospheric slab in the order of -

487   100K result in a gravitational response of 16 mGal (Fig. 12c) and for a -200 K anomaly in the

488   order of 21 mGal (Fig. 12d). Both the composition and the thermal variation influence the

489   density and consequently the gravity response. However, the thermal component is a much

490   larger contributor.

491   For the three approaches (section 3, 4.1 and 4.2) a measurable gravity effect of the subducting

492   slab segments is observable. The independent slab segments are distinguishable to a certain

493   degree with the exception of the bivergent slab configuration in the Eastern Alps (Fig. 6, and

494   11) and the model containing converted density from seismic velocities (Fig 4) , while the slab

495   configurations cannot be separated at satellite altitude (Appendix). Forward calculated gravity

496   anomalies from converted density distribution suggest a gravitational signal of the slab

497   segments in the order of 40 mGal which corresponds to a density contrast of 20 to 40 kg/m^3 in

498   the models with predefined slab geometry. The models with a Tecton like composition suggest

499   a gravity effect of the slab segments in the order of only 16 mGal, corresponding to a density

500   contrast of 20 kg/m^3 in the simple model. Increasing the compositional difference with a Tecton

501   composition suggests a gravity signal in order of 30 mGal and is in line with the converted

502   density model.

503   All three methods show a positive gravity signal contribution, which can be related to sub-

504   crustal density variations for approach 1 and to predefined sub-crustal slab segments for

505   approach 2 & 3, up to 40 mGal to the Alpine gravity field. That is significant in comparison to

506   the observed Bouguer Anomaly with a minimum of ~-200 mGal. If this contribution is not

507   considered, a significant part of the gravity signal is attributed to crustal thickness or intra-

508   crustal sources. Due to the long-wavelength appearance of the gravity effect, that might not be

509   relevant for small-scale or local studies, the effect is only seen as a shift. For gravity models of

510   larger areas (e.g. Eastern Alps) or even the entire regions that should not be neglected. For one,

511   estimates of crustal thickness or the mass distribution are significantly biased, and placing the

512   Alps in the geodynamic context of the surrounding requires a careful and complete

513   consideration of all sources in order to provide realistic density distribution required for

514   geodynamic models (e.g. Reuber et al., 2019).

515   **6 Conclusions**

516 We have addressed the potential gravity effect of proposed slab segments in the Alpine region

517 using three different modelling approaches.

518 • Converted density from seismic tomography: In the resulting gravity signal the imprint

519 of slab segments is visible, however, distinguishing between the different and

520 independent slab segments is not possible.

521 • Models with predefined slab segments are dependent on the assigned density contrast

522 and volume as well as on the predefined positions of the slab segments. The gravity

523 signal caused by the slab segments are sharp and can be separated for the different slab

524 segments for the gravity field at the surface. Significant gravity contributions from slab

525 segments below 200 – 250 km to the Alpine gravity are unlikely.

526 • Combined petrophysical-geophysical modelling results in the most complex models.

527 The calculated density variation within the slab is rather small compared to the density

528 contrast between lithosphere and sub lithosphere. The density distribution within the

529 slabs, and consequently the gravity field, is highly influenced by the slab composition

530 and thermal structure.

531 Sub-crustal density variation (approach 1) and predefined slab segments (approach 2 & 3)

532 suggest a positive sub-crustal gravity contribution of up to 40 mGal. Even though this might be

533 considered as an end of the envelope calculations, this value is significant, even compared to

534 the observed Bouger anomaly low of -200 mGal along the Alps. Previous studies compensated

535 this effect by lithosphere thickness and/or intra-crustal sources, future studies should

536 incorporate subducting slab structures in order to provide a meaningful representation of the

537 geodynamic complex Alpine area. Precise estimations of the slab density structure require a

538 correct crustal density and crustal thickness model. With the integration of further observables,

539 it might be possible to judge on the correct slab configuration beneath the Alps. Furthermore,

540 future studies based on the AlpArray Network will be of high interest in better defining slab

541 geometries as well as their properties.

Competing interests

The authors declare that they have no conflict of interest.

Author contributions

ML carried out the gravity modelling, visualized and interpreted the results and prepared the first manuscript draft. JE supervised the gravity modelling and interpretation, designed the original research project, acquisition of the financial support for the project leading to this publication and writing (reviewing and editing). TM defined the slab configurations based on tectonic and seismological knowledge and writing (reviewing and editing). AE created and provided the surface wave tomography model MeRE2020 and writing (reviewing and editing).

Acknowledgment

The authors thank the reviewers, Carla Braitenberg and an anonymous referee for their valuable suggestions, which helped to improve the manuscript significantly.

This study is part of the projects "Integrierte 3D Modellierung des Schwere- und Temperaturfelds zum Verständnis von Rheologie und Deformation der Alpen und ihrer Vorlandbecken - INTEGRATE" and "Surface Wavefield Tomography of the Alpine Region to Constrain Slab Geometries, Lithospheric Deformation and Asthenospheric Flow in the Alpine Region" funded by German Research Foundation (DFG) in the SPP Mountain Building Processes in 4D.

We thank the developer of open scientific Software which were utilized in this study: tesseroids (Uieda et al., 2016), LitMod 3D (Fullea et al., 2009 and Afonso et al., 2008) and Generic Mapping Tools (GMT) (Wessel et al., 2013; Wessel & Luis, 2017).

References

564   Afonso, J. C., Fernandez, M., Ranalli, G., Griffin, W. L., & Connolly, J. A. D. (2008). Integrated
565   geophysical-petrological modeling of the lithosphere and sublithospheric upper mantle:
566   Methodology and applications. Geochemistry, Geophysics, Geosystems, 9(5).
567

568   Amante, C., & Eakins, B. W. (2009). ETOPO1 arc-minute global relief model: procedures, data
569   sources and analysis.
570

571   Artemieva, I. M. (2019). Lithosphere structure in Europe from thermal isostasy. Earth-Science
572   Reviews, 188, 454-468.
573

574   Babuška, V., Plomerova, J., & Granet, M. (1990). The deep lithosphere in the Alps: a model
575   inferred from P residuals. Tectonophysics, 176(1-2), 137-165.
576

577   Beller, S., Monteiller, V., Operto, S., Nolet, G., Paul, A., & Zhao, L. (2018). Lithospheric
578   architecture of the South-Western Alps revealed by multiparameter teleseismic full-waveform
579   inversion. Geophysical Journal International, 212(2), 1369-1388.
580

581   Bouman, J., Ebbing, J., Fuchs, M., Sebera, J., Lieb, V., Szwillus, W., ... & Novak, P. (2016).
582   Satellite gravity gradient grids for geophysics. Scientific reports, 6(1), 1-11.
583

584   Braitenberg, C. (2015). Exploration of tectonic structures with GOCE in Africa and across-
585   continents. International Journal of Applied Earth Observation and Geoinformation, 35, 88-95.
586

587   Channell, J. E. T., & Horvath, F. (1976). The African/Adriatic promontory as a
588   palaeogeographical premise for Alpine orogeny and plate movements in the Carpatho-Balkan
589   region. Tectonophysics, 35(1-3), 71-101.
590

591   Connolly, J. A. D. (2009). The geodynamic equation of state: what and how. Geochemistry,
592   Geophysics, Geosystems, 10(10).
593

594   Dewey, J. F., Helman, M. L., Knott, S. D., Turco, E., & Hutton, D. H. W. (1989). Kinematics
595   of the western Mediterranean. Geological Society, London, Special Publications, 45(1), 265-283.
596

597   Ebbing, J., Braitenberg, C., & Götze, H. J. (2001). Forward and inverse modelling of gravity
598   revealing insight into crustal structures of the Eastern Alps. Tectonophysics, 337(3-4), 191-208.
599

600   Ebbing, J., Braitenberg, C., & Götze, H. J. (2006). The lithospheric density structure of the
601   Eastern Alps. Tectonophysics, 414(1-4), 145-155.
602

603   El‐Sharkawy, A., Meier, T., Lebedev, S., Behrmann, J., Hamada, M., Cristiano, L., ... & Köhn,
604   D. (2020). The Slab Puzzle of the Alpine‐Mediterranean Region: Insights from a new, High‐
605   Resolution, Shear‐Wave Velocity Model of the Upper Mantle. Geochemistry, Geophysics,
606   Geosystems, e2020GC008993.
607

608   Fichtner, A., van Herwaarden, D. P., Afanasiev, M., Simutė, S., Krischer, L., Çubuk-Sabuncu,
609   Y., ... & Trampert, J. (2018). The collaborative seismic earth model: Generation 1. Geophysical
610   research letters, 45(9), 4007-4016.
611

612   Frisch, W. (1979). Tectonic progradation and plate tectonic evolution of the Alps.
613   Tectonophysics, 60(3-4), 121-139.
614

615 Fullea, J., Afonso, J. C., Connolly, J. A. D., Fernandez, M., García-Castellanos, D., & Zeyen,
616 H. (2009). LitMod3D: An interactive 3-D software to model the thermal, compositional,
617 density, seismological, and rheological structure of the lithosphere and sublithospheric upper
618 mantle. Geochemistry, Geophysics, Geosystems, 10(8).

620 Fullea, J., Fernàndez, M., Afonso, J. C., Vergés, J., & Zeyen, H. (2010). The structure and
621 evolution of the lithosphere–asthenosphere boundary beneath the Atlantic–Mediterranean
622 Transition Region. Lithos, 120(1-2), 74-95.

624 Ganguly, J., Freed, A. M., & Saxena, S. K. (2009). Density profiles of oceanic slabs and
625 surrounding mantle: Integrated thermodynamic and thermal modeling, and implications for the
626 fate of slabs at the 660 km discontinuity. Physics of the Earth and Planetary Interiors, 172(3-4),
627 257-267.

629 Götze, H. J., Lahmeyer, B., Schmidt, S., & Strunk, S. (1994). The lithospheric structure of the
630 Central Andes (20–26 S) as inferred from interpretation of regional gravity. In Tectonics of the
631 southern Central Andes (pp. 7-21). Springer, Berlin, Heidelberg.

633 Götze, H. J., & Krause, S. (2002). The Central Andean gravity high, a relic of an old subduction
634 complex?. Journal of South American Earth Sciences, 14(8), 799-811.

636 Götze, H. J., & Pail, R. (2018). Insights from recent gravity satellite missions in the density
637 structure of continental margins–With focus on the passive margins of the South
638 Atlantic. Gondwana Research, 53, 285-308.

640 Grad, M., Tiira, T., & ESC Working Group. (2009). The Moho depth map of the European
641 Plate. Geophysical Journal International, 176(1), 279-292.

643 Griffin, W. L., O'reilly, S. Y., Afonso, J. C., & Begg, G. C. (2009). The composition and
644 evolution of lithospheric mantle: a re-evaluation and its tectonic implications. Journal of
645 Petrology, 50(7), 1185-1204.

647 Gutknecht, B. D., Götze, H. J., Jahr, T., Jentzsch, G., & Mahatsente, R. (2014). Structure and
648 state of stress of the Chilean subduction zone from terrestrial and satellite-derived gravity and
649 gravity gradient data. Surveys in Geophysics, 35(6), 1417-1440.

651 Handy, M. R., Schmid, S. M., Bousquet, R., Kissling, E., & Bernoulli, D. (2010). Reconciling
652 plate-tectonic reconstructions of Alpine Tethys with the geological–geophysical record of
653 spreading and subduction in the Alps. Earth-Science Reviews, 102(3-4), 121-158.

655 Handy, M. R., Ustaszewski, K., & Kissling, E. (2015). Reconstructing the Alps–Carpathians–
656 Dinarides as a key to understanding switches in subduction polarity, slab gaps and surface
657 motion. International Journal of Earth Sciences, 104(1), 1-26.

659 Hawkesworth, C. J., Waters, D. J., & Bickle, M. J. (1975). Plate tectonics in the Eastern Alps.
660 Earth and Planetary Science Letters, 24(3), 405-413.

662 Hetényi, G., Plomerová, J., Bianchi, I., Exnerová, H. K., Bokelmann, G., Handy, M. R., ... &
663 AlpArray-EASI Working Group. (2018). From mountain summits to roots: Crustal structure of
664 the Eastern Alps and Bohemian Massif along longitude 13.3 E. Tectonophysics, 744, 239-255.
665

Holzrichter, N., & Ebbing, J. (2016). A regional background model for the Arabian Peninsula from modeling satellite gravity gradients and their invariants. Tectonophysics, 692, 86-94.

Hua, Y., Zhao, D., & Xu, Y. (2017). P wave anisotropic tomography of the Alps. Journal of Geophysical Research: Solid Earth, 122(6), 4509-4528.

Isaak, D. G., Anderson, O. L., Goto, T., & Suzuki, I. (1989). Elasticity of single-crystal forsterite measured to 1700 K. Journal of Geophysical Research: Solid Earth, 94(B5), 5895-5906.

Isaak, D. G. (1992). High-temperature elasticity of iron-bearing olivines. Journal of Geophysical Research: Solid Earth, 97(B2), 1871-1885.

Karato, S. I. (1993). Importance of anelasticity in the interpretation of seismic tomography. Geophysical Research Letters, 20(15), 1623-1626.

Karousová, H., Plomerová, J., & Babuška, V. (2013). Upper-mantle structure beneath the southern Bohemian Massif and its surroundings imaged by high-resolution tomography. Geophysical Journal International, 194(2), 1203-1215.

Kästle, E. D., El-Sharkawy, A., Boschi, L., Meier, T., Rosenberg, C., Bellahsen, N., ... & Weidle, C. (2018). Surface wave tomography of the alps using ambient-noise and earthquake phase velocity measurements. Journal of Geophysical Research: Solid Earth, 123(2), 1770-1792.

Kästle, E. D., Rosenberg, C., Boschi, L., Bellahsen, N., Meier, T., & El-Sharkawy, A. (2020). Slab break-offs in the Alpine subduction zone. International Journal of Earth Sciences, 1-17.

Kincaid, C., & Olson, P. (1987). An experimental study of subduction and slab migration. Journal of Geophysical Research: Solid Earth, 92(B13), 13832-13840.

Kissling, E., Schmid, S. M., Lippitsch, R., Ansorge, J., & Fügenschuh, B. (2006). Lithosphere structure and tectonic evolution of the Alpine arc: new evidence from high-resolution teleseismic tomography. Geological Society, London, Memoirs, 32(1), 129-145.

Kogan, M. G., & McNutt, M. K. (1993). Gravity field over northern Eurasia and variations in the strength of the upper mantle. Science, 259(5094), 473-479.

Koulakov, I., Kaban, M. K., Tesauro, M., & Cloetingh, S. A. P. L. (2009). P-and S-velocity anomalies in the upper mantle beneath Europe from tomographic inversion of ISC data. Geophysical Journal International, 179(1), 345-366.

Le Breton, E., Handy, M. R., Molli, G., & Ustaszewski, K. (2017). Post-20 Ma motion of the Adriatic Plate: New constraints from surrounding orogens and implications for crust-mantle decoupling. Tectonics, 36(12), 3135-3154.

Lippitsch, R., Kissling, E., & Ansorge, J. (2003). Upper mantle structure beneath the Alpine orogen from high-resolution teleseismic tomography. Journal of Geophysical Research: Solid Earth, 108(B8).

716 Lüschen, E., Lammerer, B., Gebrande, H., Millahn, K., Nicolich, R., & TRANSALP Working
717 Group. (2004). Orogenic structure of the Eastern Alps, Europe, from TRANSALP deep seismic
718 reflection profiling. Tectonophysics, 388(1-4), 85-102.

720 Lüschen, E., Borrini, D., Gebrande, H., Lammerer, B., Millahn, K., Neubauer, F., ... &
721 TRANSALP Working Group. (2006). TRANSALP—deep crustal Vibroseis and explosive
722 seismic profiling in the Eastern Alps. Tectonophysics, 414(1-4), 9-38.

724 Lyu, C., Pedersen, H. A., Paul, A., Zhao, L., & Solarino, S. (2017). Shear wave velocities in
725 the upper mantle of the Western Alps: new constraints using array analysis of seismic surface
726 waves. Geophysical Journal International, 210(1), 321-331.

728 Mahatsente, R. (2019). Plate Coupling Mechanism of the Central Andes Subduction: Insight
729 from Gravity Model. Journal of Geodetic Science, 9(1), 13-21.

731 McDonough, W. F., & Sun, S. S. (1995). The composition of the Earth. Chemical geology,
732 120(3-4), 223-253.

734 McKenzie, D., & Fairhead, D. (1997). Estimates of the effective elastic thickness of the
735 continental lithosphere from Bouguer and free air gravity anomalies. Journal of Geophysical
736 Research: Solid Earth, 102(B12), 27523-27552.

738 Mitterbauer, U., Behm, M., Brückl, E., Lippitsch, R., Guterch, A., Keller, G. R., ... &
739 Šumanovac, F. (2011). Shape and origin of the East-Alpine slab constrained by the ALPASS
740 teleseismic model. Tectonophysics, 510(1-2), 195-206.

742 Nocquet, J. M., & Calais, E. (2004). Geodetic measurements of crustal deformation in the
743 Western Mediterranean and Europe. Pure and applied geophysics, 161(3), 661-681.

745 Piromallo, C., & Morelli, A. (2003). P wave tomography of the mantle under the Alpine‐
746 Mediterranean area. Journal of Geophysical Research: Solid Earth, 108(B2).

748 Reuber, G., Meier, T., Ebbing, J., El-Sharkawy, A., & Kaus, B. (2019, January). Constraining
749 the dynamics of the present-day Alps with 3D geodynamic inverse models-model version 0.2.
750 In Geophysical Research Abstracts (Vol. 21).

752 Root, B. C. (2020). Comparing global tomography-derived and gravity-based upper mantle
753 density models. Geophysical Journal International, 221(3), 1542-1554.

755 Schmid, S. M., Fügenschuh, B., Kissling, E., & Schuster, R. (2004). Tectonic map and overall
756 architecture of the Alpine orogen. Eclogae Geologicae Helvetiae, 97(1), 93-117.

758 Serpelloni, E., Vannucci, G., Anderlini, L., & Bennett, R. A. (2016). Kinematics,
759 seismotectonics and seismic potential of the eastern sector of the European Alps from GPS and
760 seismic deformation data. Tectonophysics, 688, 157-181.

762 Spada, M., Bianchi, I., Kissling, E., Agostinetti, N. P., & Wiemer, S. (2013). Combining
763 controlled-source seismology and receiver function information to derive 3-D Moho
764 topography for Italy. Geophysical Journal International, 194(2), 1050-1068.

766 Spakman, W., & Wortel, R. (2004). A tomographic view on western Mediterranean
767 geodynamics. In The TRANSMED atlas. The Mediterranean region from crust to mantle (pp.
768 31-52). Springer, Berlin, Heidelberg.
769
770 Spooner, C., Scheck-Wenderoth, M., Götze, H. J., Ebbing, J., & Hetényi, G. (2019). Density
771 distribution across the Alpine lithosphere constrained by 3-D gravity modelling and relation to
772 seismicity and deformation. Solid Earth, 10(6), 2073-2088.
773
774 Stampfli, G. M., & Borel, G. D. (2002). A plate tectonic model for the Paleozoic and Mesozoic
775 constrained by dynamic plate boundaries and restored synthetic oceanic isochrons. Earth and
776 Planetary Science Letters, 196(1-2), 17-33.
777
778 Tašárová, Z. A. (2007). Towards understanding the lithospheric structure of the southern
779 Chilean subduction zone (36 S–42 S) and its role in the gravity field. Geophysical Journal
780 International, 170(3), 995-1014.
781
782 Tiberi, C., Diament, M., Lyon Caen, H., & King, T. (2001). Moho topography beneath the
783 Corinth Rift area (Greece) from inversion of gravity data. Geophysical Journal
784 International, 145(3), 797-   808.
785
786 Uieda, L., Barbosa, V. C., & Braitenberg, C. (2016). tesseroids: Forward-modeling
787 gravitational fields in spherical coordinates. Geophysics, 81(5), F41-F48.
788
789 Vacher, P., Mocquet, A., & Sotin, C. (1998). Computation of seismic profiles from mineral
790 physics: the importance of the non-olivine components for explaining the 660 km depth
791 discontinuity. Physics of the Earth and Planetary Interiors, 106(3-4), 275-298.
792
793 Vrabec, M., & Fodor, L. (2006). Late Cenozoic tectonics of Slovenia: structural styles at the
794 Northeastern corner of the Adriatic microplate. In The Adria microplate: GPS geodesy,
795 tectonics and hazards (pp. 151-168). Springer, Dordrecht.
796
797 Wang, Y., He, Y., Lu, G., & Wen, L. (2020). Seismic, thermal and compositional structures of
798 the stagnant slab in the mantle transition zone beneath southeastern China. Tectonophysics,
799 775, 228208.
800
801 Webb, S. J. (2009). The use of potential field and seismological data to analyze the structure of
802 thelithosphere beneath southern Africa (Doctoral dissertation).
803
804 Wessel, P., Smith, W. H., Scharroo, R., Luis, J., & Wobbe, F. (2013). Generic mapping tools:
805 improved version released. Eos, Transactions American Geophysical Union, 94(45), 409-410.
806
807 Wessel, P., & Luis, J. F. (2017). The GMT/MATLAB Toolbox. Geochemistry, Geophysics,
808 Geosystems, 18(2), 811-823.
809
810 Workman, R. K., & Hart, S. R. (2005). Major and trace element composition of the depleted
811 MORB mantle (DMM). Earth and Planetary Science Letters, 231(1-2), 53-72.
812
813 Zeyen, H., & Fernàndez, M. (1994). Integrated lithospheric modeling combining thermal,
814 gravity, and local isostasy analysis: Application to the NE Spanish Geotransect. Journal of
815 Geophysical Research: Solid Earth, 99(B9), 18089-18102.
816

817 Zhao, L., Paul, A., Malusà, M. G., Xu, X., Zheng, T., Solarino, S., ... & Aubert, C. (2016).
818 Continuity of the Alpine slab unraveled by high-resolution P wave tomography. Journal of
819 Geophysical Research: Solid Earth, 121(12), 8720-8737.
820
821 Zingerle, P., Pail, R., Gruber, T., & Oikonomidou, X. (2019). The experimental gravity field
822 model XGM2019e.
823

824 **Appendix A Gravity Gradients at satellite height**

825 For all Alpine density models presented above (section 3, 4,1 and 4.2) we have also calculated

826 gravity gradients at a station height of 225 km. This station height corresponds to the second

827 mission phase of GOCE (Gravity field and steady-state ocean circulation explorer) carried out

828 by ESA (European Space Agency).

829 We anticipated that gravity gradients measured by the GOCE satellite mission are sensitive to

830 the slab segments in the Alpine region. Our result show, that the long wavelength signal of the

831 different present slab segments contributes to a large-scale gravity response where the different

832 contributor cannot be separated. Therefore, we conclude that against our anticipation gravity

833 gradients at satellite height are in fact not sensitive to the Alpine slab configuration. We show

834 here, the gravity gradients (mainly the gzz component) for completeness.

835 Measured gravity gradients from the GOCE mission (Bouman et al., 2016), which were

836 corrected for topography and bathymetry ranges from 2.5 to -2.5 E at satellite altitude of 225

837 km height (Fig. 13). A negative gravity anomaly of -2.5 E in the gzz component is observed

838 equivalent to the vertical gz component (Fig. 13). However, no clear sign for subducting

839 lithosphere can be observed in any component of the gravity gradient tensor.
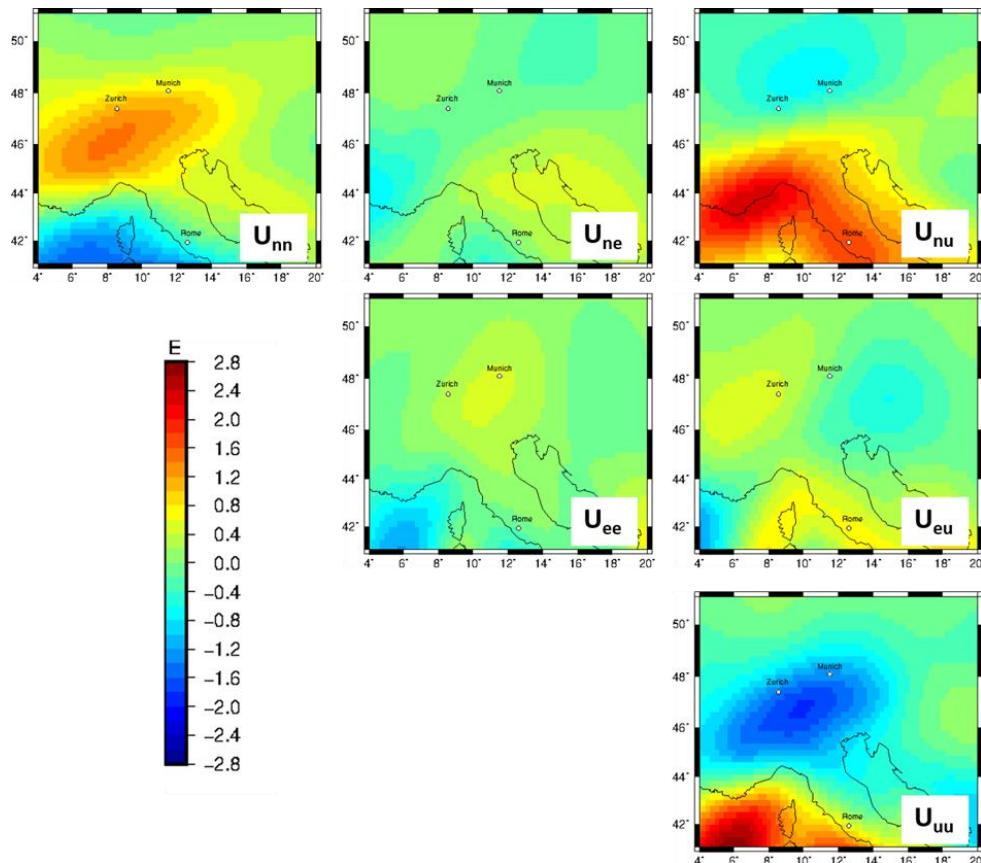
840
841 *Figure 13 GOCE gradients at 225 km height after Bouman et al. (2016) corrected for topography and bathymetry with a 5°*
842 *extension to remove far filed effects. The gravity gradients are presented in a North-East-Up coordinate system.*

843 The forward calculated gzz component at 225 km station height from a density model (section

844 3) with converted densities ranges from -3.5 E to 0.7 E (Fig. 14). A positive gravity signal of

845 about 0.5 E in the Apennine and Alpine region is observed which could be linked to subducting

846 slab segments. However, it is impossible to separate specific slab segments.
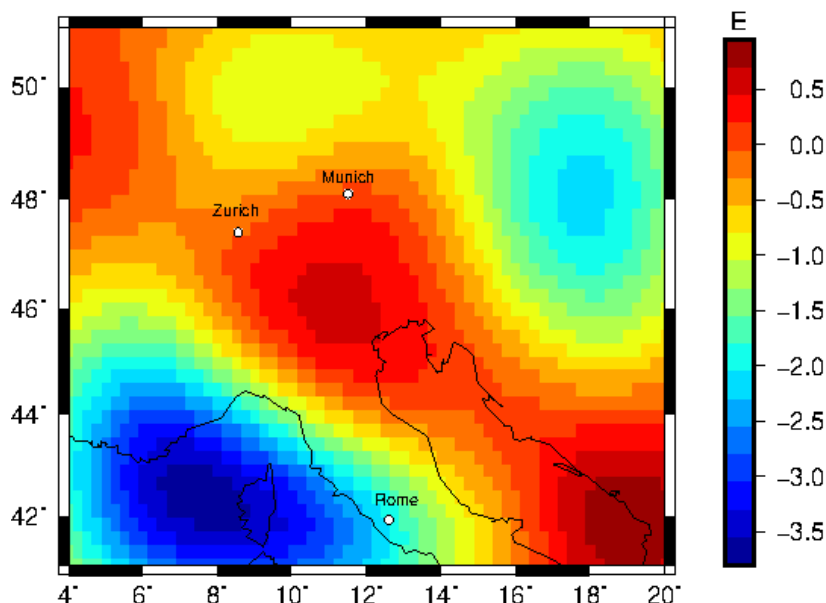
847
848 *Figure 14 Forward calculated gzz gravity signal from relative density distribution converted from relative seismic velocities*
849 *using a conversion factor of 0.3.for the at 225 km station height.*

850   Forward calculated tesseroid models (section 4.1) for slab configuration 1 and 2 with a constant

851   density contrast of 60 kg/m³ and a constant thickness of 80 km result in a less sharp gravity

852   signal for the gzz component at a station height of 225 km (Fig. 15) compared to the gz

853   component at station height of 6040 m (Fig. 6). The gravity signal for the gzz component is in

854   the range of 0.8 E to 1 E. At satellite altitude the gravity signal is observed as a large area with

855   a positive gravity effect for Configuration 1 and 2. The contribution of the different slab

856   segments to this positive gravity effect is not distinguishable. The only recognizable difference

857   is the size of this positive gravity signal. Configuration 1 shows a smaller anomaly, due to a

858   lower volume of subducting material in the Eastern Alps.

859
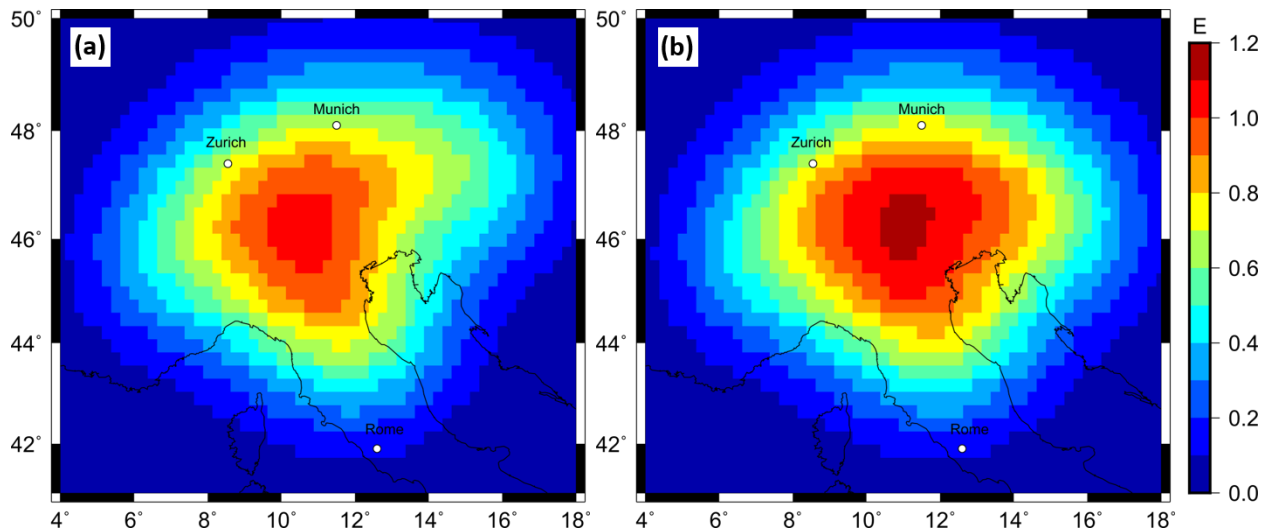
*Figure 15 Forward calculated gzz gravity signal at a station height of 225 km from predefined sub-crustal slab geometries with a content density contrast of 60 kg/ m³ and a constant thickness of 80 km. **(a)** slab configuration of hypothesis 1 **(b)** slab configuration of hypothesis 2.*

863   In Addition, the signal strength for the forward calculated gzz component show the same

864   dependency of signal strength to the density contrast and slab thickness (Fig. 16) as the gz

865   component (Fig. 7). The signal strength of the gzz component ranges for the 12 different

866   combinations from 0.3 E to 2 E (Fig. 16). The gravity signal cannot be separated and affiliated

867   to a certain slab segment. The gzz gradient signal shows a large blurry gravity high over the

868   Alps, which thins out to the edges.
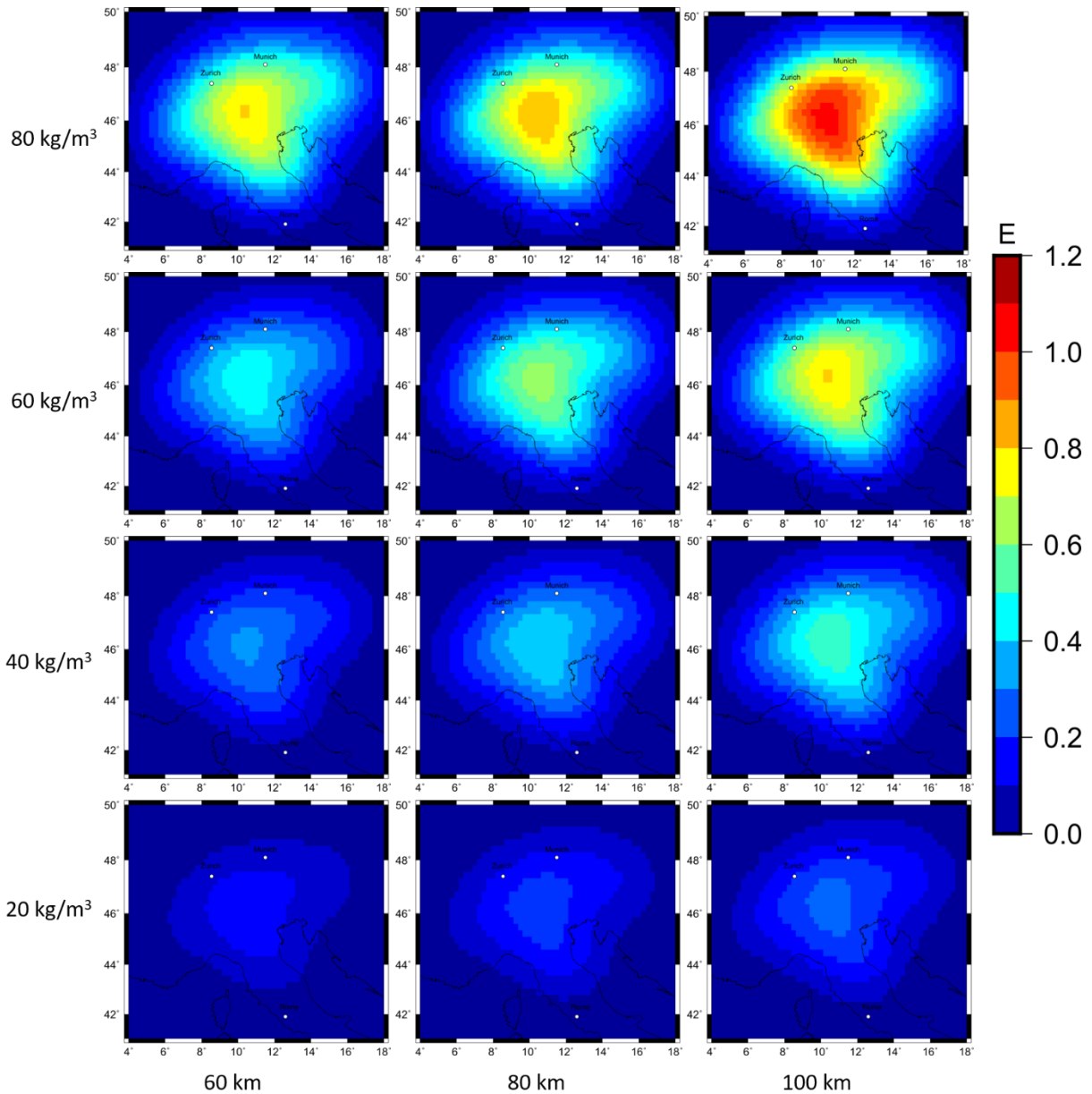
869
870 *Figure 16 Forward calculated gzz gravity signal for 12 different combination of density contrast and slab thickness at a station*
871 *height of 225 km for sub-crustal slab configuration 1.*

872 The gravity effect for the LitMod models (section 4.2) with the slab Configuration 1 shows in

873 the lithosphere domain a signal strength of about 0.05 E, while the sub lithospheric gravity

874 signal is in the range of 0.1 E for the gzz component at satellite altitude of 225 km height. The

875 combined gravity signal is in the order of 0.14 E (Fig. 17). A Proterozoic slab produces a larger

876 amplitude in signal strength, however the different slab segments can again not be separated

877 (Fig. 18).
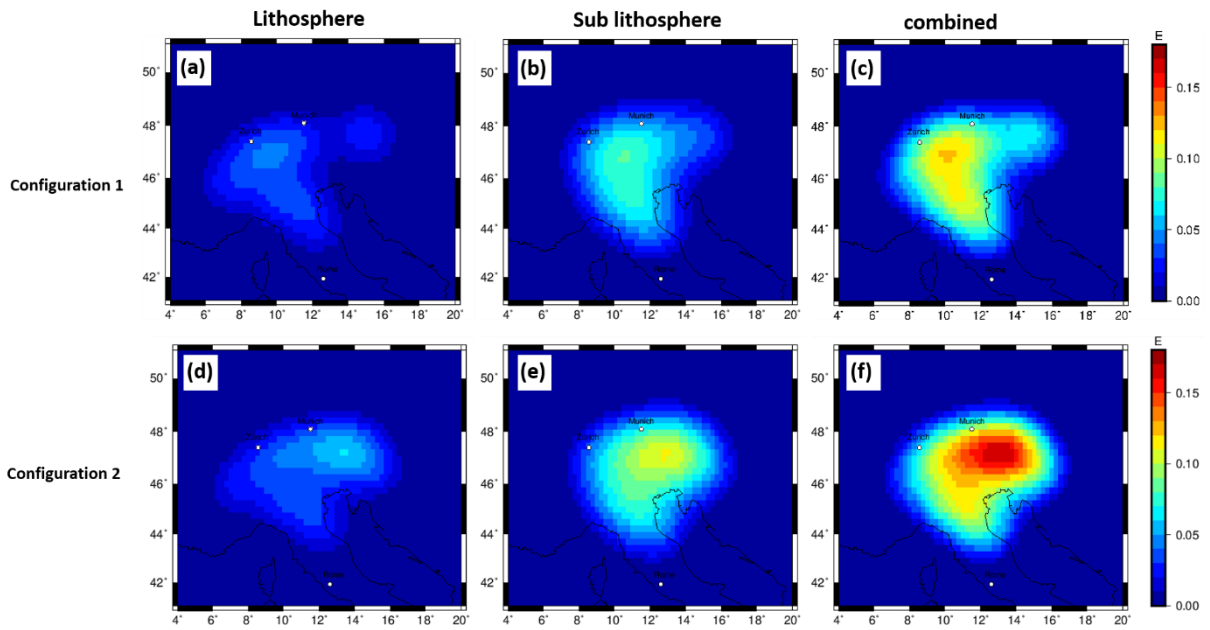
Figure 17 forward calculated gzz gravity signal at satellite altitude of 225 km based on LitMod models with tecton like compositions in the lithosphere and PUM and DMM compositions in the sub lithosphere (M_1, M_2, M_3, M_4) with an additional thermal anomaly of -100° K for the sub-lithospheric slab segment, for predefined slab Configuration to the background model M_0. **(a)-(c)** for Configuration 1. **(d)-(f)** for Configuration 2. Topographic and crustal effects are nullified.
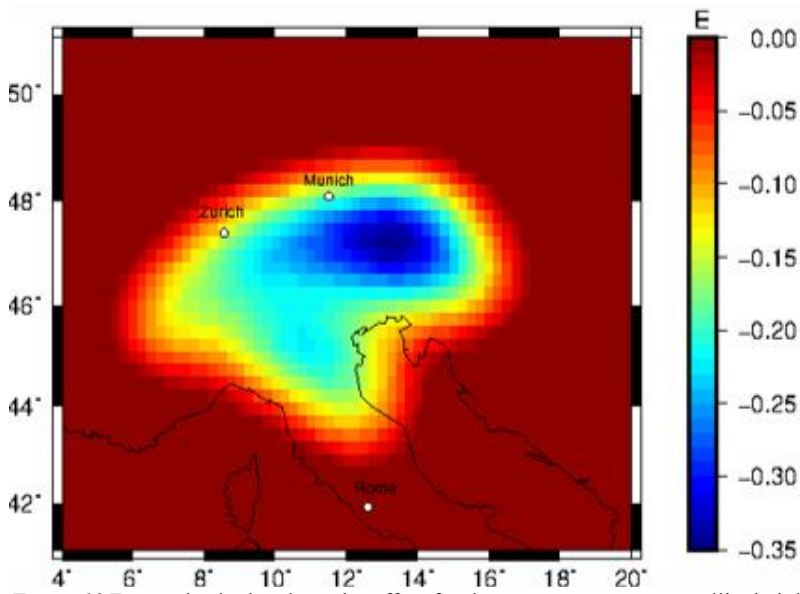
Figure 18 Forward calculated gravity effect for the gzz component at satellite height of a Proterozoic lithospheric slab segment to a Tecton compositional surrounding mantle for Configuration 2 obtained by calculating the residual between M_8 and M_0.